PAPER

Streamer-to-filament transition in pulsed nanosecond atmospheric pressure discharge: 2D numerical modeling

To cite this article: Bin Zhang *et al* 2023 *Plasma Sources Sci. Technol.* **32** 115014

View the article online for updates and enhancements.

Streamer-to-filament transition in pulsed nanosecond atmospheric pressure discharge: 2D numerical modeling

Bin Zhang[1,5] ⓘ**, Yifei Zhu**[2] ⓘ**, Xiaobing Zhang**[1,*] ⓘ**, Nikolay Popov**[3] ⓘ**, Thomas Orriere**[4] ⓘ**, David Z Pai**[5] ⓘ **and Svetlana M Starikovskaia**[5,*] ⓘ

[1] School of Energy and Power Engineering, Nanjing University of Science and Technology, Nanjing 210094, People's Republic of China
[2] School of Electrical Engineering, Xi'an Jiaotong University, Xi'an 710049, People's Republic of China
[3] Skobeltsyn Institute of Nuclear Physics, Moscow State University, Moscow 119991, Leninsky gory, Russia
[4] Département Fluides, Thermique et Combustion, Institut Pprime (CNRS UPR 3346, Université de Poitiers, ENSMA), bd Marie et Pierre Curie, Téléport 2, BP 30179 F, 86962 Chasseneuil Futuroscope, France
[5] Laboratory of Plasma Physics (CNRS, Ecole Polytechnique, Univ. Paris-Sud, Observatoire de Paris, Sorbonne Université, l'Institut Polytechnique de Paris), Ecole Polytechnique, route de Saclay, 91128 Palaiseau, France

E-mail: zhangxb680504@163.com and svetlana.starikovskaia@lpp.polytechnique.fr

CrossMark

Abstract

The streamer-to-filament transition in air at atmospheric pressure, in a nanosecond pin-to-pin discharge, is studied by a 2D model. The main aim is to implement a kinetic scheme providing a sharp electron density increase to the 2D PASSKEy code, to validate the results on the available experimental data, and to investigate the mechanisms responsible for the transition. Results show that after the formation of a conductive channel across the discharge gap, two discharge modes appear during a few nanoseconds: a glow phase, with a relatively homogeneous distribution with the electron density of 1.0×10^{14} cm^{-3}, and a filamentary phase, with the electron density of 1.0×10^{18} cm^{-3}. Two filaments appear at the cathode and anode respectively, and propagate towards the middle of the gap with a velocity of about $1.1 \cdot 10^7$ cm s^{-1}, forming a narrow channel. Simultaneously, the gas temperature increases from 350 to 2800 K. The diameter of the channel at the middle gap decreases from 210 to 90 μm. Dissociation and ionization of the electronically excited states of molecules N$_2$(A$^3\sum_u^+$, B$^3\Pi_g$, a$'^1\sum_u^-$, C$^3\Pi_u$), and ionization of ground and electronically excited states of O and N atoms are the most important processes for the transition. Numerical results also reveal the influence of the memory effect (pre-heating, pre-ionization, and pre-dissociation) from previous pulses on the streamer-to-filament transition.

Keywords: plasma, kinetics, 2D modeling, streamer-to-filament transition, nanoseconds

---

* Authors to whom any correspondence should be addressed.

1. Introduction

At atmospheric pressure, the most often appearing and the most studied form of a transient plasma of high-voltage nanosecond discharges between two electrodes is referred to as a 'streamer'. In a recent review [1] streamers are defined as 'propagating ionization fronts with self-organized field enhancement at their tips'. Under fixed high-voltage pulse parameters and constant temperature, the streamer's diameter is inversely proportional to the gas pressure. This statement has been confirmed through both experimental observations and computational simulations [2]. With increase of the high voltage amplitude, the diameter of a streamer increases. According to measurements [3], the typical streamer diameter in atmospheric pressure air is around 0.2 mm at voltage amplitudes ranging from 5 to 20 kV, expanding to approximately 3 mm at about 100 kV. The electron densities in streamer channels in the atmospheric pressure air are within the range $10^{13} - 4 \times 10^{15}$ cm^{-3} [1].

In some experimental scenarios, the streamer diameter abruptly decreases within a few nanoseconds to a few tens of microns, while the electron density simultaneously increases by more than four orders of magnitude. This contracted channel on the axis of the streamer is referred to as a filament, and the process is known as the 'streamer-to-filament transition' [4–9]. It should be noted that this transition has been observed in both pin-to-pin [4], pin-to-plane [5] volumetric discharges and in surface dielectric barrier [6] discharge.

In volumetric pin-to-pin pulse discharges, three distinct stages can be identified [10]: (i) the streamer mode, which characterizes streamer initiation and propagation until the discharge gap closes [11–13]; (ii) the glow mode, which follows the streamer's traversal of the gap and is characterized by uniform distribution of plasma parameters along the discharge gap axis [8, 10, 11, 14]; (iii) the third stage with a formation of a narrow strongly ionized plasma channel on the axis of the discharge [4, 10]. Since the plasma state in this narrow channel is close to local thermal equilibrium (LTE), it was proposed to call this stage thermal spark [4]. The streamer-to-filament transition represents the evolution from the stage (i) towards the initial phase of stage (iii). This transition occurs via the stage (ii) in open electrode discharges, whereas it is absent in surface dielectric barrier discharges (SDBDs). To flexibly control the discharge mode and meet the requirements of different applications, a more in-depth understanding of the mechanism of the streamer-to-filament transition is needed.

The contraction of the channel appearing at the end of the glow phase is a key element of the streamer-to-filament transition phenomenon. The decrease in the diameter of the developed glow discharge is accompanied by a sharp increase in the electron density. The electron density up to 4.0×10^{18} cm^{-3} was measured across two pin-shaped electrodes in pure N$_2$ and N$_2$/H$_2$O mixtures [9]. A fully ionized plasma with the electron density above 1.0×10^{19} cm^{-3} was observed in a nanosecond repetitively pulsed (thermal spark) discharge in air with a 2 mm pin-to-pin gap [4]. During the glow phase,

the authors observed two filaments, one forming at each electrode, that propagate toward the middle of the inter-electrode gap. During this transition, the discharge contracted toward the channel axis, and induced a dramatic rise of the gas temperature, from 1200 K to 36 000 K in less than 5 ns [8]. In the case of SDBDs, the streamer-to-filament transition in a single pulse was demonstrated in a wide range of pressures and gas mixtures [6, 15, 16]. Similar to volume discharges, the transition started in the vicinity of the electrode, specifically the high-voltage electrode in the case of SDBDs. The typical time of filamentation was about 1 ns or less in the pressure range of 2–10 bar. The electron density increased from about 1.0×10^{15} cm^{-3} in the streamer phase to 1.0×10^{19} cm^{-3} in the filament phase, and the diameter of the channel decreased from 200 to 20 μm [17]. The emission spectrum during the transition was first dominated by the molecular bands of N$_2$ and then continuous wavelength (cw) emission with the distinct appearance of broadened lines of atoms (N, O) and ionized atoms (N$^+$) [8, 17].

Few attempts have been made to numerically simulate transition processes with such a high ionization degree. Known 2D modeling has described mainly nanosecond glow discharges or the glow-to-spark transition. For example, a 2D model to study the glow-to-spark transition in a pin-to-pin discharge at atmospheric pressure in air was developed in [12, 13]. In the calculations, two streamers that develop from the electrodes propagate in opposite directions, forming a conductive channel. Parametric calculations with a given heat release due to fast gas heating demonstrated the electron density increases to $\sim 10^{16}$ cm^{-3}, with hydrodynamic effects noticeable at the microsecond timescale.

A 0D model explaining the properties of filamentary nanosecond discharges revealed that the dissociation and ionization of electronically excited states N$_2$(B$^3\Pi_g$, C$^3\Pi_u$) by electron impact promotes the ionization process [18]. The electron density increases rapidly from 1.0×10^{15} to 1.0×10^{19} cm^{-3} in nitrogen at 6 bar, with an initial reduced electric field of 230 Td. Another 0D modeling study [19] emphasizes the importance of the ionization of the excited electronic states of O and N for the transition to thermal spark, which plays the main role in plasma ionization for $n_e > 1.0 \times 10^{16}$ cm^{-3}.

This transition always occurs over a few nanoseconds. First, streamers cross the gap and form a continuous plasma channel, which we will refer to as the 'glow' phase. After the glow phase, which is spatially homogeneous and non-equilibrium, the plasma channel shrinks in radius with a sharp increase in electron density. In the present work, for clarification, we refer to this initially constricted plasma channel with corresponding high electron density as the 'filament', although at this point the plasma is not yet at LTE. Subsequently, the plasma attains very high electron densities (10^{18}–10^{19} cm^{-3}) and temperatures (30 000–50 000 K) that are sufficient for reaching LTE. We refer to the transient fully ionized plasma channel as the 'thermal spark' at true LTE conditions. We consider here a streamer-to-filament transition as the initial stage of the transition to the thermal spark.

The objective of this paper is to gain insight into the mechanism of the streamer-to-filament transition in ambient air using a simplified kinetic scheme coupled to a 2D PASSKEy code. We will model a nanosecond discharge in a relatively simple pin-to-pin geometry and benchmark our code against experimental results from [20]. In this work, we only focus on the formation of the filament as the first step of the formation of the thermal spark.

2. Experimental setup

The experimental results presented here originate from [20]. Most of the description of the experimental setup can be found in [21], including the validation of the current–voltage measurements and the setup for optical emission spectroscopy. Additional details are as follows. Imaging was performed using the same instrumentation as for spectroscopy, with the same time resolution of 3 ns, except with the diffraction grating positioned to deliver zero-order light to the camera. The entrance slit of the spectrometer was fully open to 5 mm, and the image projected onto the camera was magnified by a factor of 4. To calculate the diameter of the discharge at a given position along the discharge axis, the luminous intensity was integrated along the radial direction, and the edges of the discharge were defined by points at which the integrated signal reached 16% and 84% of the maximum value. These points were assumed to represent the standard deviation of a Gaussian profile with a corresponding full-width half-maximum that we defined as the discharge diameter.

The rotational temperature of the $N_2(C^3\Pi_u)$ state was determined by fitting measured spectra of the band transitions $N_2(C^3\Pi_u, v' = 1 \rightarrow B^3\Pi_g, v'' = 3)$ and $N_2(C^3\Pi_u, v' = 0 \rightarrow B^3\Pi_g, v'' = 2)$ to modeled spectra produced by SPECAIR [22] or MassiveOES [23]. As far as at $T < 1000$ K the *RT* relaxation occurs in less than 10 collisions [24], the characteristic time of this process at atmospheric pressure does not exceed 0.5 ns [25]. Thus, the determination of the gas temperature on the basis of rotational spectra under given conditions is justified [26, 27].

3. Model description

The computational framework is designed to model the streamer-to-filament transition in a pin-to-pin configuration. According to the experiments (see figure 42 from [20]), the plasma possesses azimuthal symmetry during both the glow and filament phases, and therefore an axisymmetric model is used here.

The 2D PASSKEy (PArallel Streamer Solver with KinEtics) code is used. The code has been used to model nanosecond surface discharges [28–31] and validated by measurements of discharge morphology, propagation velocity, voltage–current curves, as well as a pin-to-plane model benchmark [32] and models of streamer-to-spark transitions [33]. Detailed mathematical formulations, the strategy for multiphysics and multiscale coupling, and validations can be found elsewhere [28, 30, 34].

3.1. Discharge model

The classical fluid model is used here, which consists of drift-diffusion reaction equations for species densities coupled with Helmholtz equations for photoionization, the electron energy equation for the mean electron energy, and Poisson's equation for the electric field. The equations are the following:

$$\frac{\partial n_i}{\partial t} + \nabla \cdot \boldsymbol{\Gamma_i} = S_i + S_{\text{ph}}, i = 1, 2, \ldots, N_{\text{total}} \tag{1}$$

$$\boldsymbol{\Gamma_i} = (q_i/|q_i|)\,\mu_i n_i \boldsymbol{E} - D_i \nabla n_i, i = 1, 2, \ldots, N_{\text{ch}} \tag{2}$$

$$\frac{\partial}{\partial t}(n_e \epsilon_m) + \nabla \cdot \boldsymbol{\Gamma_\epsilon} = -|q_e| \cdot \boldsymbol{\Gamma_e} \cdot \boldsymbol{E} - P(\epsilon_m) \tag{3}$$

$$\boldsymbol{\Gamma_\epsilon} = -n_e \epsilon_m \mu_\epsilon \boldsymbol{E} - D_\epsilon \nabla(n_e \epsilon_m) \tag{4}$$

$$\nabla(\varepsilon_0 \varepsilon_r \nabla \Phi) = -\sum_{i=1} q_i n_i \tag{5}$$

$$\boldsymbol{E} = -\nabla \Phi \tag{6}$$

where n_i, q_i, $\boldsymbol{\Gamma_i}$, μ_i and D_i are the number density, charge, flux, mobility and diffusion coefficients for each species i, respectively. The source function S_i includes production and loss terms due to gas phase reactions and is calculated with detailed kinetic processes. The photoionization source term for electrons and positive ions S_{ph} is calculated via three-exponential Helmholtz equations. The parameters of the Helmholtz equations for air have been given in [35]. The photoionization is important only at the stage of propagation of the streamer. The mean electron energy is ϵ_m, and μ_ϵ and D_ϵ are the electron mobility and diffusion coefficient, respectively. $P(\epsilon_m)$ represents the power lost by electrons in collisions. The dependence on the mean electron energy ϵ_m of the rate coefficients of electron collision reactions, electron swarm parameters, and power loss by electrons is obtained by solving the Boltzmann equation in a two-term approximation using BOLSIG+ software [36]. Φ is the electric potential, $\boldsymbol{E}$ the electric field, ε_0 is the vacuum permittivity, and ε_r is the relative permittivity. A set of Euler equations was solved for gas temperature and density variations. The coupling strategy between the plasma and Euler equations has been described in detail in [30].

3.2. Kinetic mechanism

It is essential to choose the right kinetic scheme for modeling the streamer-to-filament transition. The reaction scheme of [29], which describes a streamer discharge and was validated for nanosecond SDBDs, as well as pin-to-pin and pin-to-plane nanosecond discharges [28, 30, 31, 33, 34], is used as a baseline.

The streamer-to-filament transition is accompanied by a sharp increase in the electron density, up to about 10^{19} cm^{-3} [17, 18, 21]. The baseline scheme mentioned above is enough for simulations at low ionization degree, with electron
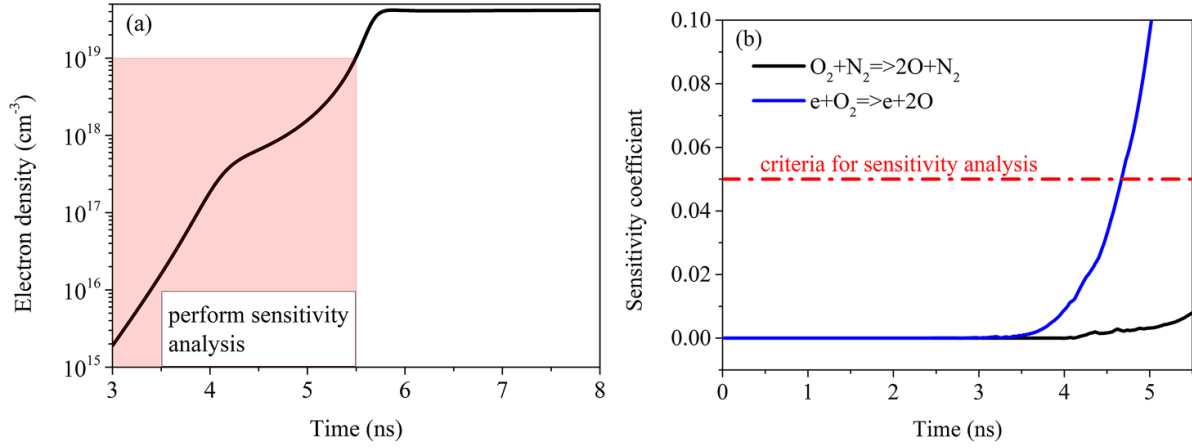
Figure 1. (a) Temporal evolution of the electron density from the 0D simulation. The red shaded region indicates the range used for sensitivity analysis. (b) Examples of the sensitivity coefficient for two reactions. The red dashed line indicates the criterion for selecting reactions for 2D modeling.

densities of about 1.0×10^{15} cm^{-3}, and should be extended to higher ionization degree. A reaction scheme based on [37] was recently extended and used in a 0D configuration, reproducing the experimental results of [38] for a nanosecond discharge and a transition from non-equilibrium to equilibrium plasma in air. Ideally, this reaction scheme would be used in our work to explore how the streamer-to-filament transition develops. However, this scheme consists of about 300 reactions, and including all of them in the 2D simulation would be too computationally expensive.

To simplify the kinetics, a sensitivity analysis was performed for the 0D model with the ZDPlasKin code [39] to check which reactions can be responsible for a sharp increase in electron density. The rate coefficients for each reaction were sequentially changed by 50%. The sensitivity coefficients are given as [40]:

$$\varphi(t)_{i,r} = \frac{c(t)_{i,r=1.5r} - c(t)_{i,r}}{c(t)_{i,r}} \quad (7)$$

where r is a reaction rate for the ith reaction. $c(t)_{i,r=1.5r}$ and $c(t)_{i,r}$ are the electron densities under study with modified and un-modified rate coefficients, respectively. The threshold for including a reaction in the 2D model was set by the condition

$$\varphi(t)_{i,r} \geqslant 0.05 \quad (8)$$

for any time instant t.

For the purpose of the 0D sensitivity analysis, we assume an initial reduced electric field. The maximum voltage (6 kV) and discharge gap (1 mm) applied in the experiment (shown later) yield an electric field of 6 kV mm^{-1}. This corresponds to an initial reduced electric field $E/N_0 = 240$ Td at a gas temperature of 300 K and pressure of $P = 1$ atm. Here, N_0 is the initial neutral particle density. Note that for the 2D calculations shown later, Poisson's equation will be solved to obtain the electric field. Figure 1(a) shows the evolution of the electron density, which sharply increases above 1.0×10^{19} cm^{-3}.

As this paper considers only initial stage of the transition, the sensitivity analysis was limited to $t \leqslant 5.5$ ns ($n_e \leqslant 10^{19}$ cm^{-3}). Processes with $\varphi(t)_{i,r} \geqslant 0.05$ were added to the baseline kinetic scheme [29].

It is important to note that in the context of 2D modeling, the changes in the electron energy distribution function (EEDF) arising from the increasing density of electronically excited species/atoms are not considered. To check how relevant is this assumption, the 0D calculations presented in figure 1(a) were replicated using the conditions outlined in the study by [19]. This particular paper investigates the impact of excited electronic states on the ionization of ambient air induced by a nanosecond discharge, employing a 0D modeling approach; the analysis accounts for dissociation, ionization, and super-elastic collisions when calculating the EEDF. A good agreement was found between the present work and results of [19]: at 200 Td, the electron density increases from $\sim 10^{16}$ cm^{-3} to $\sim 10^{19}$ cm^{-3} during 4 ns in our calculations and during 2 ns in the calculations [19]. These results can be readily explained by the more intricate kinetics of excited nitrogen atoms, considering that ionization initiating from eight excited N-atoms was taken into consideration in the study by [19].

To reduce the computing cost, we only consider the excited states N(^{2}D, ^{2}P) and O(^{1}D, ^{1}S), as well as the ground states N(^{4}S) and O(^{3}P). Ionization reactions from excited atoms by electron impact begin to work with an electron density of about 1.0×10^{17} cm^{-3} [19]. The role of a given excited atom state in ionization is determined by the ratio of the constants of ionization and quenching by electrons. Therefore, the reverse processes of excitation (de-excitation) by electron impact are important. The resulting scheme consisting of 92 reactions was implemented into the 2D PASSKEy code.

We extended the baseline kinetic scheme based on the sensitivity analysis. The detailed reactions, rate coefficients, cross-section data, and references are listed in table 1.

Table 1. Kinetic scheme for the streamer-to-filament transition in air.

No.	Reaction	Rate constant[a]	References
R1	$e + N_2 \Rightarrow 2e + N_2^+$	$f(\sigma, \epsilon)$	[41]
R2	$e + O_2 \Rightarrow 2e + O_2^+$	$f(\sigma, \epsilon)$	[42]
R3	$e + O_2 \Rightarrow 2e + O + O^+$	$f(\sigma, \epsilon)$	[42]
R4	$e + NO \Rightarrow 2e + NO^+$	$f(\sigma, \epsilon)$	[43]
R5	$e + O \Rightarrow 2e + O^+$	$f(\sigma, \epsilon)$	[44]
R6	$e + N \Rightarrow 2e + N^+$	$f(\sigma, \epsilon)$	[45]
R7	$e + N_2(A^3\sum_u^+) \Rightarrow 2e + N_2^+$	$f(\sigma, \epsilon)$	[46]
R8	$e + N_2(B^3\Pi_g) \Rightarrow 2e + N_2^+$	$f(\sigma, \epsilon)$	[46]
R9	$e + N_2(C^3\Pi_u) \Rightarrow 2e + N_2^+$	$f(\sigma, \epsilon)$	[46]
R10	$e + N_2(a'^1\sum_u^-) \Rightarrow 2e + N_2^+$	$f(\sigma, \epsilon)$	[46]
R11	$e + N(^2D) \Rightarrow 2e + N^+$	$f(\sigma, \epsilon)$	[45]
R12	$e + N(^2P) \Rightarrow 2e + N^+$	$f(\sigma, \epsilon)$	[45]
R13	$e + O(^1D) \Rightarrow 2e + O^+$	$f(\sigma, \epsilon)$	[44]
R14	$e + O(^1S) \Rightarrow 2e + O^+$	$f(\sigma, \epsilon)$	[44]
R15	$e + O_2 \Rightarrow e + O + O + 0.8\,eV$	$f(\sigma, \epsilon)$	[47]
R16	$e + O_2 \Rightarrow e + O + O(^1D) + 1.26\,eV$	$f(\sigma, \epsilon)$	[47]
R17	$e + N_2 \Rightarrow e + N + N(^2D)$	$f(\sigma, \epsilon)$	[48, 49]
R18	$e + N_2(A^3\sum_u^+) \Rightarrow e + N + N$	$f(\sigma, \epsilon)$	[46]
R19	$e + N_2(B^3\Pi_g) \Rightarrow e + N + N(^2D)$	$f(\sigma, \epsilon)$	[46]
R20	$e + N_2(C^3\Pi_u) \Rightarrow e + N + N(^2D)$	$f(\sigma, \epsilon)$	[46]
R21	$e + N_2(a'^1\sum_u^-) \Rightarrow e + N + N(^2D)$	$f(\sigma, \epsilon)$	[46]
R22	$e + N_2 \Leftrightarrow e + N_2(A^3\sum_u^+)$	$f(\sigma, \epsilon)$	[50]
R23	$e + N_2 \Leftrightarrow e + N_2(B^3\Pi_g)$	$f(\sigma, \epsilon)$	[50]
R24	$e + N_2 \Leftrightarrow e + N_2(C^3\Pi_u)$	$f(\sigma, \epsilon)$	[50]
R25	$e + N_2 \Leftrightarrow e + N_2(a'^1\sum_u^-)$	$f(\sigma, \epsilon)$	[50]
R26	$e + N_2(A^3\sum_u^+) \Leftrightarrow e + N_2(B^3\Pi_g)$	$f(\sigma, \epsilon)$	[46]
R27	$e + N_2(A^3\sum_u^+) \Leftrightarrow e + N_2(a'^1\sum_u^-)$	$f(\sigma, \epsilon)$	[46]
R28	$e + N_2(A^3\sum_u^+) \Leftrightarrow e + N_2(C^3\Pi_u)$	$f(\sigma, \epsilon)$	[46]
R29	$e + N_2(B^3\Pi_g) \Leftrightarrow e + N_2(C^3\Pi_u)$	$f(\sigma, \epsilon)$	[46]
R30	$e + N_2(B^3\Pi_g) \Leftrightarrow e + N_2(a'^1\sum_u^-)$	$f(\sigma, \epsilon)$	[46]
R31	$e + N \Leftrightarrow e + N(^2D)$	$f(\sigma, \epsilon)$	[45]
R32	$e + N \Leftrightarrow e + N(^2P)$	$f(\sigma, \epsilon)$	[45]
R33	$e + N(^2D) \Leftrightarrow e + N(^2P)$	$f(\sigma, \epsilon)$	[45]
R34	$e + O \Leftrightarrow e + O(^1D)$	$f(\sigma, \epsilon)$	[44]
R35	$e + O \Leftrightarrow e + O(^1S)$	$f(\sigma, \epsilon)$	[44]
R36	$e + O(^1D) \Leftrightarrow e + O(^1S)$	$f(\sigma, \epsilon)$	[44]
R37	$e + O_2 \Rightarrow O + O^-$	$f(\sigma, \epsilon)$	[51]
R38	$e + O_2 + O_2 \Rightarrow O_2 + O_2^-$	$2.0 \times 10^{-29}(300/T_e)$	[2]
R39	$e + N_2^+ \Rightarrow N + N(^2D) + 3.44\,eV$	$1.8 \times 10^{-7}(300/T_e)^{0.39} \times 0.46$	[52]
R40	$e + N_2^+ \Rightarrow N(^2D) + N(^2D) + 1.06\,eV$	$1.8 \times 10^{-7}(300/T_e)^{0.39} \times 0.46$	[52]
R41	$e + N_2^+ \Rightarrow N + N(^2P) + 2.25\,eV$	$1.8 \times 10^{-7}(300/T_e)^{0.39} \times 0.08$	[52]
R42	$e + O_2^+ \Rightarrow O + O + 6.95\,eV$	$1.95 \times 10^{-7}(300/T_e)^{0.7} \times 0.32$	[52]
R43	$e + O_2^+ \Rightarrow O + O(^1D) + 4.99\,eV$	$1.95 \times 10^{-7}(300/T_e)^{0.7} \times 0.43$	[52]
R44	$e + O_2^+ \Rightarrow O(^1D) + O(^1D) + 3.02\,eV$	$1.95 \times 10^{-7}(300/T_e)^{0.7} \times 0.2$	[52]
R45	$e + O_2^+ \Rightarrow O(^1D) + O(^1S) + 0.8\,eV$	$1.95 \times 10^{-7}(300/T_e)^{0.7} \times 0.05$	[52]
R46	$e + NO^+ \Rightarrow N + O + 2.71\,eV$	$4.2 \times 10^{-7}(300/T_e)^{0.85} \times 0.2$	[24]
R47	$e + NO^+ \Rightarrow N(^2D) + O + 0.33\,eV$	$4.2 \times 10^{-7}(300/T_e)^{0.85} \times 0.8$	[24]
R48	$e + N_4^+ \Rightarrow N_2 + N_2(C^3\Pi_u) + 3.49\,eV$	$2.0 \times 10^{-6}(300/T_e)^{0.5}$	[53]
R49	$e + O_4^+ \Rightarrow O + O + O_2 + 4.6\,eV$	$4.2 \times 10^{-6}(300/T_e)^{0.48}$	[53]
R50	$N^+ + N_2 \Rightarrow N + N_2^+$	$1.66 \times 10^{-12}T_{gas}^{0.5}\exp(-12000/T_{gas})$	[54]
R51	$N + N_2^+ \Rightarrow N^+ + N_2 + 1.07\,eV$	$2.27 \times 10^{-7}T_{gas}^{-0.83}\exp(-3048/T_{gas})$	[55]
R52	$N_2 + O^+ \Rightarrow O + N_2^+$	$1.49 \times 10^{-12}T_{gas}^{0.36}\exp(-22800/T_{gas})$	[54]
R53	$O + N_2^+ \Rightarrow N_2 + O^+ + 1.96\,eV$	$8.6 \times 10^{-11}T_{gas}^{-0.3}\exp(-926/T_{gas})$	[55]
R54	$N + NO^+ \Rightarrow O + N_2^+$	$1.2 \times 10^{-10}\exp(-35500/T_{gas})$	[54]
R55	$O + N_2^+ \Rightarrow N + NO^+ + 3.1\,eV$	$1.58 \times 10^{-9}T_{gas}^{-0.43}\exp(-478/T_{gas})$	[55]
R56	$N + O_2^+ \Rightarrow O_2 + N^+$	$1.44 \times 10^{-10}T_{gas}^{0.14}\exp(-28600/T_{gas})$	[54]

(Continued.)

Table 1. (Continued.)

No.	Reaction	Rate constant[a]	References
R57	$O_2 + N^+ \Rightarrow N + O_2^+ + 2.46\,\text{eV}$	$2.61\times10^{-14}T_{\text{gas}}^{0.98}\exp(2030/T_{\text{gas}})$	[55]
R58	$N_2 + O_2^+ \Rightarrow O_2 + N_2^+$	$1.64\times10^{-11}\exp(-40700/T_{\text{gas}})$	[54]
R59	$O_2 + N_2^+ \Rightarrow N_2 + O_2^+ + 3.51\,\text{eV}$	$2.39\times10^{-10}T_{\text{gas}}^{-0.44}\exp(-379/T_{\text{gas}})$	[55]
R60	$N_2^+ + N_2 + N_2 \Rightarrow N_4^+ + N_2 + 1.05\,\text{eV}$	5.0×10^{-29}	[53]
R61	$N_2^+ + N_2 + O_2 \Rightarrow N_4^+ + O_2 + 1.05\,\text{eV}$	5.0×10^{-29}	[53]
R62	$N_4^+ + O_2 \Rightarrow O_2^+ + N_2 + N_2 + 2.45\,\text{eV}$	2.5×10^{-10}	[53]
R63	$O_2^+ + N_2 + N_2 \Rightarrow O_2^+N_2 + N_2$	$9.0\times10^{-31}(300/T_{\text{gas}})^2$	[53]
R64	$O_2^+N_2 + N_2 \Rightarrow O_2^+ + N_2 + N_2$	4.3×10^{-10}	[2]
R65	$O_2^+N_2 + O_2 \Rightarrow O_4^+ + N_2$	1.0×10^{-9}	[2]
R66	$O_2^+ + O_2 + N_2 \Rightarrow O_4^+ + N_2 + 0.43\,\text{eV}$	$2.4\times10^{-30}(300/T_{\text{gas}})^{3.2}$	[53]
R67	$O_2^+ + O_2 + O_2 \Rightarrow O_4^+ + O_2 + 0.43\,\text{eV}$	$2.4\times10^{-30}(300/T_{\text{gas}})^{3.2}$	[53]
R68	$O^- + O \Rightarrow e + O_2$	1.4×10^{-10}	[24]
R69	$O_2^- + O \Rightarrow e + O_2 + O$	1.5×10^{-10}	[2]
R70	$O_2^- + O_4^+ \Rightarrow O_2 + O_2 + O_2$	1.0×10^{-7}	[2]
R71	$O_2^- + O_4^+ + N_2 \Rightarrow 3\,O_2 + N_2$	2.0×10^{-25}	[2]
R72	$O_2^- + O_4^+ + O_2 \Rightarrow 3\,O_2 + O_2$	2.0×10^{-25}	[2]
R73	$O_2^- + O_2^+ + N_2 \Rightarrow 2\,O_2 + N_2$	2.0×10^{-25}	[2]
R74	$O_2^- + O_2^+ + O_2 \Rightarrow 2\,O_2 + O_2$	2.0×10^{-25}	[2]
R75	$O^- + N_2^+ \Rightarrow O + N + N$	$2.0\times10^{-7}(300/T_{\text{gas}})^{0.5}$	[56]
R76	$N_2(A^3\sum_u^+) + O_2 \Rightarrow N_2 + O + O + 1.06\,\text{eV}$	1.7×10^{-12}	[53]
R77	$N_2(A^3\sum_u^+) + O_2 \Rightarrow N_2 + O_2 + 6.17\,\text{eV}$	$4.3\times10^{-14}T_{gas}^{0.5}$	[56]
R78	$N_2(A^3\sum_u^+) + O \Rightarrow NO + N(^2D) + 0.55\,\text{eV}$	4.0×10^{-11}	[57]
R79	$N_2(B^3\Pi_g) + O_2 \Rightarrow N_2 + O + O + 2.35\,\text{eV}$	3.0×10^{-10}	[53]
R80	$N_2(B^3\Pi_g) + N_2 \Rightarrow N_2(A^3\sum_u^+) + N_2 + 1.17\,\text{eV}$	1.0×10^{-11}	[56]
R81	$N_2(B^3\Pi_g) + O \Rightarrow NO + N(^2D) + 1.77\,\text{eV}$	3.0×10^{-10}	[58]
R82	$N_2(C^3\Pi_u) + N_2 \Rightarrow N_2(B^3\Pi_g) + N_2 + 3.66\,\text{eV}$	1.0×10^{-11}	[53]
R83	$N_2(C^3\Pi_u) + O_2 \Rightarrow N_2 + O + O(^1D) + 4.83\,\text{eV}$	1.4×10^{-10}	[53, 59]
R84	$N_2(C^3\Pi_u) + O_2 \Rightarrow N_2 + O + O + 5.86\,\text{eV}$	1.6×10^{-10}	[53, 59]
R85	$N_2(C^3\Pi_u) \Rightarrow N_2(B^3\Pi_g) + h\nu$	2.45×10^7	[2]
R86	$N_2(C^3\Pi_u) + O \Rightarrow NO + N(^2D) + 6.45\,\text{eV}$	3.0×10^{-10}	[58]
R87	$N_2(a'^1\sum_u^-) + N_2 \Rightarrow N_2(B^3\Pi_g) + N_2 + 1.06\,\text{eV}$	2.0×10^{-13}	[60]
R88	$N_2(a'^1\sum_u^-) + O_2 \Rightarrow N_2 + O + O + 3.28\,\text{eV}$	2.8×10^{-11}	[60]
R89	$N_2(a'^1\sum_u^-) + O \Rightarrow NO + N(^2D) + 2.83\,\text{eV}$	3.0×10^{-10}	[58]
R90	$O(^1D) + O_2 \Rightarrow O + O_2 + 0.33\,\text{eV}$	$3.3\times10^{-11}\exp(67/T_{\text{gas}})$	[53]
R91	$O(^1D) + N_2 \Rightarrow O + N_2 + 1.37\,\text{eV}$	$1.8\times10^{-11}\exp(107/T_{\text{gas}})$	[53]
R92	$N(^2D) + N_2 \Rightarrow N + N_2(v) + 2.35\,\text{eV}$	$4.52\times10^{-14}T_{\text{gas}}^{0.68}\exp(-1438/T_{\text{gas}})$	[61]
R93	$O + NO \Rightarrow N + O_2$	$2.5\times10^{-15}T_{gas}\exp(-19439/T_{\text{gas}})$	[55]
R94	$N + O_2 \Rightarrow O + NO$	$1.07\times10^{-14}T_{gas}\exp(-3147/T_{\text{gas}})$	[55]
R95	$O + N_2 \Rightarrow N + NO$	$2.89\times10^{-10}\exp(-38455/T_{\text{gas}})$	[55]
R96	$N + NO \Rightarrow O + N_2$	$6.61\times10^{-11}\exp(-504/T_{\text{gas}})$	[55]

[a] Rate constants are given in $1\,\text{s}^{-1}$, $\text{cm}^3\,\text{s}^{-1}$ and $\text{cm}^6\,\text{s}^{-1}$, and T_{gas} and T_e are the gas and electron temperatures (in units of K), respectively. The arrow $\Rightarrow$ indicates only the forward reaction is calculated, and $\Leftrightarrow$ means both the forward and backward reactions are included.

3.3. Geometry, initial and boundary conditions

Figure 2 illustrates the schematic diagram of the experiment [20, 21], where a pin-to-pin electrode configuration with a 1 mm discharge gap was utilized. The upper electrode was powered by a nanosecond pulse with +6 kV peak voltage and 20 ns duration, while the electrode below was grounded. The radius of curvature of both needle electrodes was 150 μm.

The discharge operated in air at atmospheric pressure. The experiments were performed in repetitive mode with a frequency of 8 kHz [20, 21], but the simulation of successive discharges is beyond the scope of this paper.

In the present model, to approximate the effect of numerous preceding discharges that can leave behind some degree of preionization, a uniformly distributed electron density of 10^9 cm^{-3} was used as the initial value. At this relatively high degree of preionization, photoionization has been found to have no effect on the results [62]. To account for the cumulative thermal effect of repeated pulses, the preheated air temperature here is set at 350 K (figure 67 of [20]), according to the temperature measurement in the experiment. Thus, the total neutral density is 2.1×10^{19} cm^{-3}.

At the anode, homogeneous Neumann conditions are chosen for the negative particle fluxes, while the positive ion fluxes are set to zero; at the cathode, all positive and negative
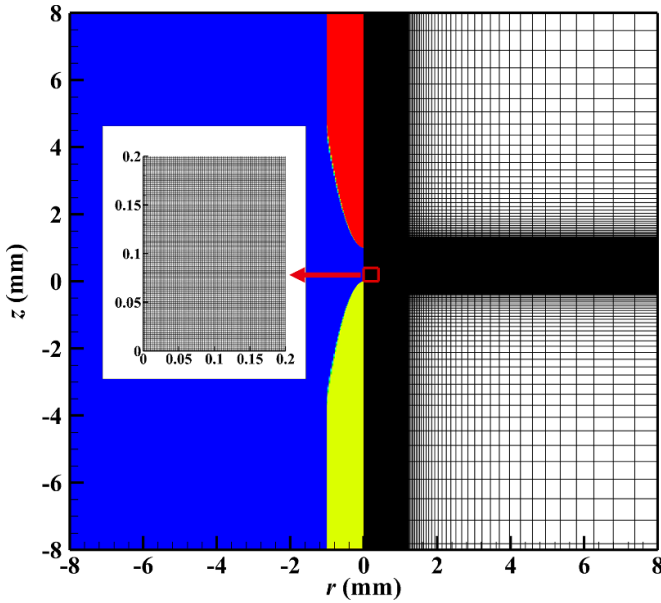
Figure 2. Geometry and mesh distribution. High-voltage electrode: red domain; grounded electrodes: yellow domain.

Figure 3. The comparison of the electric current between the experimental data (figure 40 of [20]) and calculated results.

charge fluxes are estimated using Neumann conditions [63]. The homogeneous Neumann condition applied to all charged particle fluxes on the cathode can be regarded as an equivalent description of the conductive current condition that facilitates and ensures the transition from a current wave propagation to a current conduction channel [63]. More detailed discussion on the validity of the Neumann boundary conditions can be found elsewhere [33, 62–65].

4. Results of plasma modeling

4.1. Electrical parameters

In order to confirm the validity of the model, the experimental waveform of the electrical current (figure 40 of [20]), which was measured by a current probe at the cathode, similar to [33] is chosen as a benchmark. The calculated current I_{total} is the integral of the current density over the cathode surface S, which can be given as:

$$I_{total} = \int_S |q_e| n_e(t) v_{dr}(t) dS \qquad (9)$$

where v_{dr} is the electron drift velocity. The direct comparison between the experimental and numerical data is shown in figure 3. Matching the experimental current pulse waveform by the modeling is challenging in general but somewhat simplified in the conditions of the present paper because of a few clearly distinguished stages of the discharge corresponding to different time intervals. Good agreement is found for the first rise and drop of the current, before 15 ns. The first sharp rise of the current at 10 ns corresponds to the formation of the conductive channel when a streamer crosses the gap, as shown in figure 4. At time instant 15 ns, the gap is closed by a thin conductive channel (filament) with a high electron density.
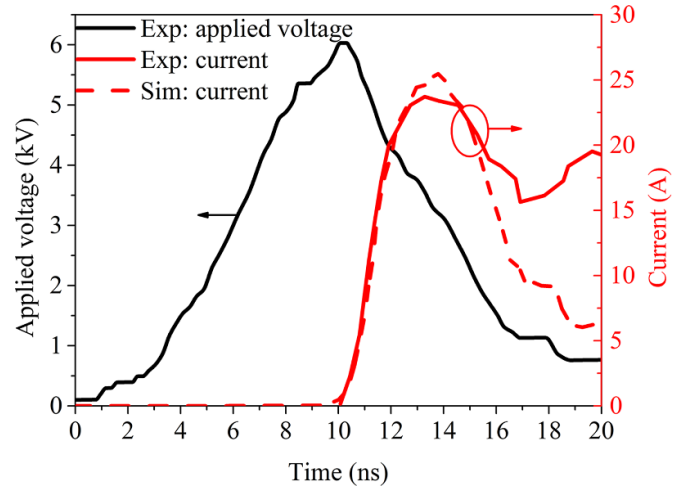
As the ionization degree n_e/N in plasma increases, the ratio of the frequency of electron–ion collisions to the frequency of electron–neutral collisions, ν_{ei}/ν_{ee}, increases. Electron–ion collisions cause additional electron momentum and energy losses, the EEDF collapses to thermal energies and becomes strongly coupled to the ion distribution function [66]. So-called Spitzer regime is installed. Under the conditions of the present work ($P = 1$ atm, $T_{gas}^0 = 350$ K) the electron-ion collisions become dominant ($\nu_{ei}/\nu_{ee} > 3$) at the electron density $n_e > 10^{18}$ cm^{-3} and the electron temperature $T_e < 3$ eV [21].

The purpose of this work was to model the initiation of filamentation process and to obtain time- and space-resolved picture of ionization in the discharge gap. A detailed analysis of the parameters of plasma channels in the Spitzer conductivity (thermal spark) mode is beyond the scope of the present paper.

4.2. Morphology properties

Figure 4 shows the electron density and reduced electric field in time and space. At the beginning of the discharge (8.6 ns), a positive streamer at the anode and a weak electron cloud at the cathode travel in opposite directions towards the gap center. At 9.2 ns, the positive streamer continues to propagate towards the cathode in the pre-ionized channel produced by the negative streamer. While the positive streamer propagates to the cathode, the electric field is high at the ionization front (figures 4(b1) and (b2)). This is a typical picture of the initial stage of development of a nanosecond pin-to-pin discharge [12, 67]. Then, the positive streamer merges with the 'corona-like' negative streamer. This is observed at 9.6 ns, when the positive streamer reaches the cathode, filling the discharge gap and forming a conductive channel. The electron density in the glow channel is about 1.0×10^{14} cm^{-3}, and the electric field is still high at about 250 Td, which is higher than the ionization threshold of air (120 Td).

Streamers can be considered as the initial breakdown stage of air in short discharge gaps. They can precede sparks, create
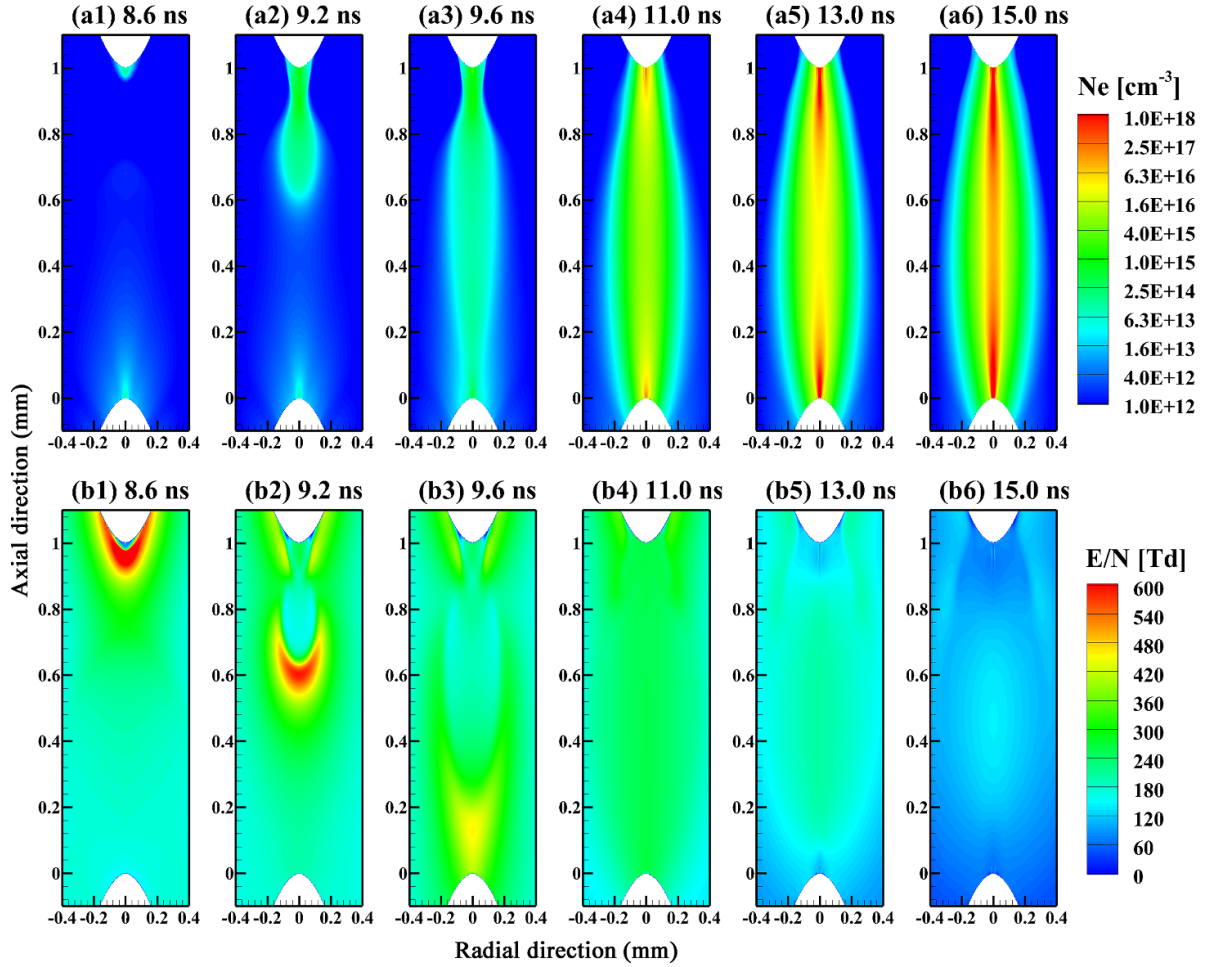
Figure 4. The evolution of the electron density and reduced electric field.

the path for leaders in lightning, and are responsible for the filamentary discharge structure in non-equilibrium plasmas at atmospheric pressure [68]. Once the streamer crosses the gap, the electron density increases dramatically at both the anode and cathode. At 11.0 ns, this high electron density distribution appearing at both electrodes can be seen as the initial stage of the filament. It should be noted that in the experiment, the filament first appears at the cathode and then the anode [4], which indicates a non-homogeneous distribution of electron density along the filament, with increasing electron density towards the cathode. In our simulation, the filaments appear at the anode and cathode nearly at the same time. Then these two initial filaments both propagate towards the gap center, shown in figures 4(a5) and (a6), forming a narrow discharge channel. The electron density is very high, at about 1.0×10^{17} cm^{-3} at the gap center and 5.0×10^{18} cm^{-3} near the electrodes (see figure 5). This high value of electron density is consistent with the experiments [4, 9, 21]. According to [69], the electric field in the channel is sensitive to the value of electron density, and decreases as the electron density rises. A similar effect, namely a decrease in the electric field near both electrodes, is clearly seen in figures 4(b5) and (b6).

Figure 5 presents the axial reduced electric field and electron density. At 9.2 ns, the high-field region, generated in front

of the streamer propagating from the high-voltage electrode, is clearly seen. The electric field after the passage is reduced considerably, but remains high during the glow phase: $E(t) \approx U(t)/d$, where $U(t)$ is the applied voltage and d is the discharge gap length. After the gap is closed, the current is constant along the discharge gap. At $t \geqslant 11$ ns, the electron density increases significantly on the axis of the discharge near the electrodes, corresponding to the formation of plasma channels with a very high ionization degree. The electric field in the corresponding regions decreases.

Will note that under the considered conditions, the duration of transition is only a few nanoseconds, and the full width at half maximum (FWHM) of the voltage pulse is less than 10 ns, both are much shorter than the characteristic gas dynamic time. During the entire discharge pulse, the E/N value changes only due to changes in the field value and dissociation of the mixture molecules. The key difference between the given conditions and the conditions under which secondary streamers are observed [70–72] is that in our case the gas density does not change as a result of hydrodynamic expansion.

The calculated streak images of the time-dependent distribution of the electron density and reduced electric field along the axis are shown in figure 6. Figure 6(a) shows that the negative streamer starts to develop before the positive streamer.
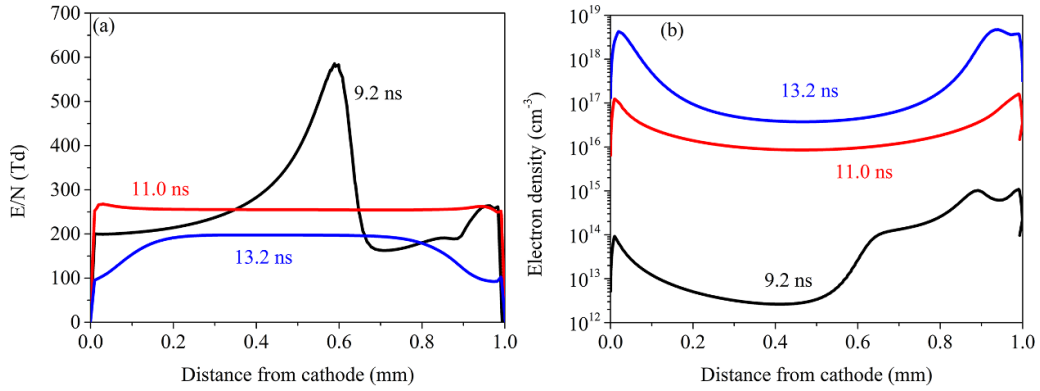
Figure 5. Axial reduced electric field and electron density distributions at different time moments 9.2, 11.0 and 13.2 ns.
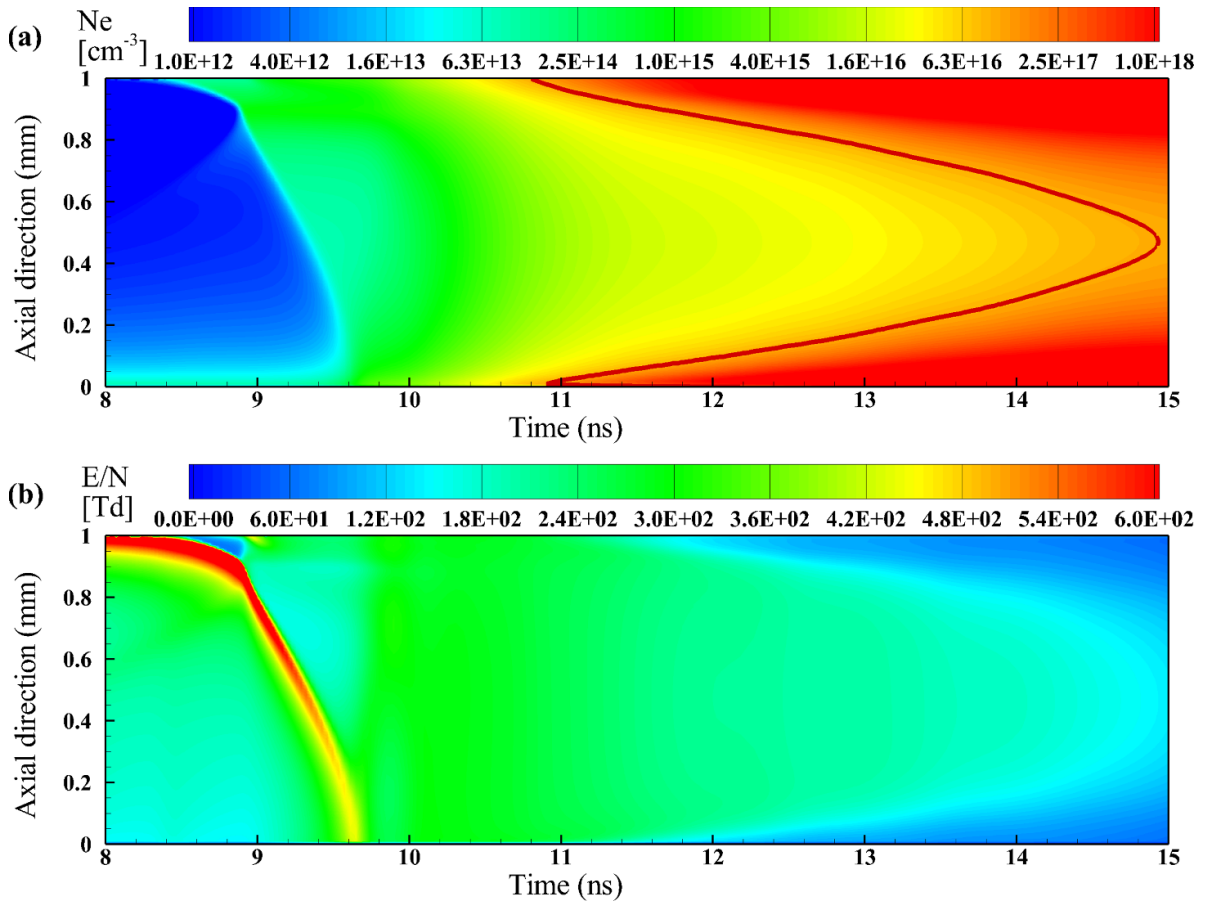

Figure 6. Simulated streak images for (a) electron density and (b) reduced electric field on the axis of the discharge. The thick red line in (a) indicates the electron density of 1.0×10^{17} cm^{-3}.

The negative streamer remains stationary as a diffuse cloud of electron density near the cathode. The positive streamer starts to propagate at about 8.6 ns at the applied voltage of 5 kV, and accelerates abruptly at about 8.8 ns. The magnitude of the electric field on the positive streamer head is stronger than for the negative streamer. The reduced electric field at the head of the positive streamer gradually decreases as it propagates closer to the cathode, as shown in figure 6(b). After the streamer crosses the gap at 9.6 ns, the electric field along the axis becomes uniform and approximately equal to

the mean electric field, which decreases with the drop of voltage. Although the applied voltage starts to drop at this time, the electric field is still high in the channel, above 250 Td. Therefore, the electron density increases sharply first at the electrodes. A filament is considered to be formed if the electron density increases to 1.0×10^{17} cm^{-3}, which is indicated by a thick red line in figure 6(a). The cathode-directed and anode-directed filaments extend from the anode and the cathode, respectively. These two filaments propagate towards the gap center almost at the same time, and merge at the gap center
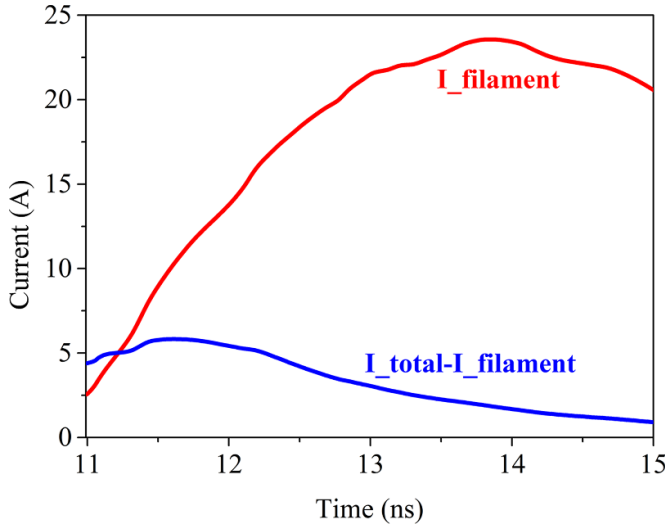
Figure 7. Temporal profile of the current components of the filament(s) and the glow.

Figure 8. $z - t$ diagram of the positive streamer and filaments as a function of time.

at 14.9 ns. The electric field strength decreases with the passage of the filaments.

The role of a constricted part of the discharge (i.e. the filaments) in the formation of the electrical current can be determined from the numerical data. During the streamer-to-filament transition, the contribution to the current by the filament(s) can be defined as:

$$I_{\text{filament}} = \int_{S(n_e \geqslant 10^{17})} |q_e| n_e(t) v_{dr}(t) \, dS \qquad (10)$$

where I_{filament} is the integral of the current density over the cathode surface where the electron density exceeds 1.0×10^{17} cm^{-3}. The currents of the filament(s) and the glow are shown in figure 7. Starting from the appearance of the filaments near the electrodes, I_{filament} increases progressively, reaching almost I_{total} at 15 ns, when the discharge gap is closed by the filaments merging at the center of the gap.

4.3. Propagation dynamics

Figure 8 presents the $z - t$ diagram of the positive streamer and the filaments, where z is the coordinate along the discharge axis. Here, the position of the positive streamer is defined by the maximum E/N on the z axis. The propagation of the positive streamer in a pin-to-pin discharge has been discussed in [12]. Figure 8 shows that during the initial propagation of the positive streamer, the velocity is almost constant at about 2.0×10^5 m s^{-1}. After the interaction between the positive and negative streamers, the positive streamer propagates with a higher speed of about 1.1×10^6 m s^{-1}.

The filaments are defined as regions where the electron density reaches above 1.0×10^{17} cm^{-3}, as indicated by the thick red line in figure 6(a). The dynamics of the cathode- and anode-directed filaments are almost the same, with an average propagation velocity of about 1.1×10^5 m s^{-1}, which is much lower than that of the streamer. From ICCD images in (figure 42 of [20]) the filament velocity can be estimated to
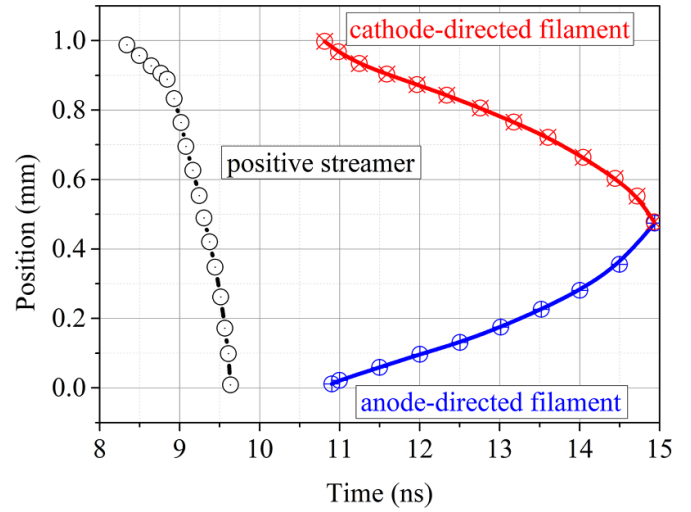
be 2×10^5 m s^{-1}. In the experiment [4], the average velocity of the filament at atmospheric pressure was about 4.0×10^4 m s^{-1}.

Will note that the filaments forming at 8 bar in a surface DBD in air propagate at 4.0×10^5 m s^{-1} [18]. According to [18], an estimate of the filament propagation velocity can be obtained by the formula $V = R_f / t_f$, where R_f is the filament radius and t_f is the filamentation time (that is, the contraction time of the current channel). With $R_f = 50$ μm and $t_f = 1$ ns, we obtain the propagation velocity $V = 5.0 \times 10^4$ m s^{-1}, which agrees with the measurement data.

The streamer-to-filament transition is accompanied by the contraction of the plasma channel. The radial distribution of the electron density in the channel can be approximated by a Gaussian function. Here, the diameter of the discharge channel D_c is defined as the FWHM, if we plot the radial distribution of electron density in normalized form, as shown in figure 9(a).

In the experiments, the diameter of the plasma channel was measured from the ICCD images, without any specific wavelength region selection. It is known for the streamer-to-filament transition that, at the stage of a streamer ($t < 9.5$ ns) and of a glow discharge ($t < 11.5$ ns) the spectra contains mainly the second positive system of molecular nitrogen. When the transition starts, the optical image of the filament is formed by continuous wavelength spectrum and the emission of atomic lines (see [6, 16], figure 50 of [20]). It should be noted that additional calculations show a good correlation between the electrical (calculated from the electron density) and optical (calculated from the density of $N_2(C^3\Pi_u)$ at earlier stages and from the density of N-atoms at later stages) diameters of the plasma filament: the difference comprises less than 10–20% and was much smaller than the changes of the diameter of the plasma channel in time and space.

Figure 9(b) presents the evolution of the calculated D_c at different distances from the cathode at times following the crossing of the gap by the streamer. The simulated results are compared with our experimental data (figure 47 of [20]) and are in a good agreement. After the gap crossing, the channel
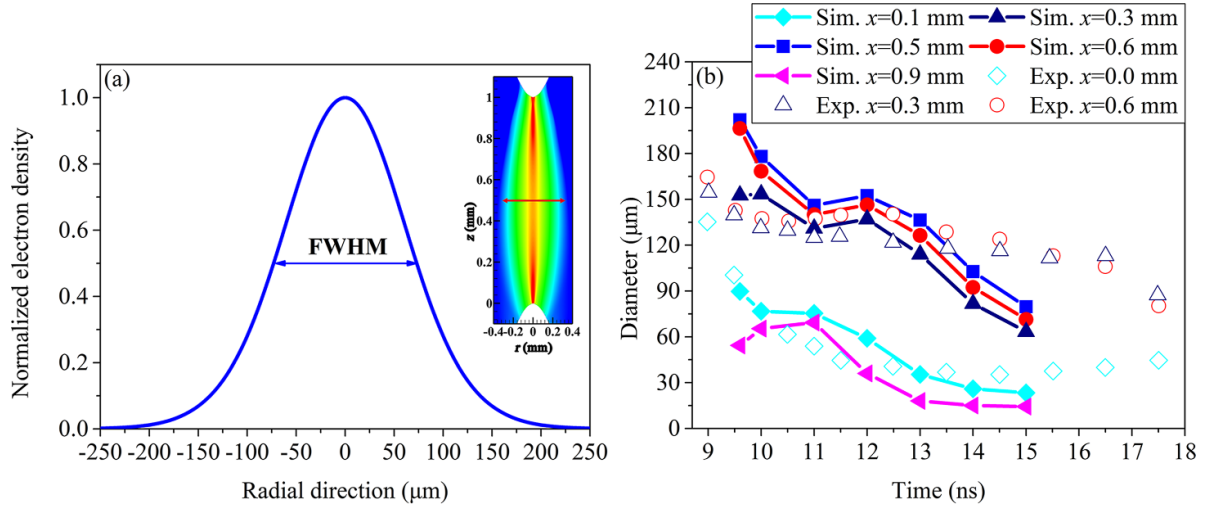
Figure 9. (a) Example of the normalized radial distribution of electron density at the gap center, indicated by a red arrow in the inserted image of the discharge. The diameter of the discharge channel D_c is defined by the FWHM. (b) Evolution of the channel diameter for different distances from the cathode. Experimental data are derived from figure 47 of [20].

diameter at the middle of the gap is 210 μm. As the filament develops, the diameter sharply reduces to 110 μm. As can be seen from the figure, the channel constriction first appears near the electrodes (0.1 and 0.9 mm), then in the rest of the discharge gap. The closer to the electrodes, the earlier the channel contraction occurs, and the smaller the diameter of the channel becomes. In the following section, it will be shown that the filamentation develops as two ionization waves appear and propagate toward each other because of changes in chemical kinetics at high E/N and specific energy density.

4.4. Transition mechanism

Figure 10 describes the time evolution of the main neutral, excited and charged species near the cathode. The electron density rapidly increases just after the positive streamer reaches the cathode (9.6 ns) and continues growing afterwards. The rate of increase in the electron density slows down after 11.3 ns (time instant for the streamer-to-filament transition), due to the increase in the recombination rate and the reduction of the electric field strength.

Over a few nanoseconds, the plasma abruptly changes from molecular to almost atomic in composition. The time evolution of N and O atoms illustrates this tendency. Up to 94 % dissociation of N_2 and 98 % dissociation of O_2 are obtained close to the cathode. Shortly after, the atoms are rapidly excited by electron impact, and the number density of the excited states of N and O increases. The ground and electronically excited atoms are ionized, and thus N^+ and O^+ become the main charged particles. This can explain the experimentally observed emission of atomic ionic species such as N^+ and O^+ when the filament forms (figure 57 of [20]).

According to the spectrum of the light emission in the wavelength range λ from 380 to 410 nm, the intensity of the $N_2(C^3\Pi_u, v'=2 \to B^3\Pi_g, v''=5)$ and $N_2^+(B^2\Sigma_u^+, v'=0 \to X^2\Sigma_g^+, v''=0)$ bands increases during the glow phase and decreases during the filament phase
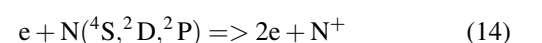
([6, 16], figure 57 of [20]). The modeled number densities of $N_2(C^3\Pi_u)$ and N_2^+ show the same trend, with the increase attributed to the excitation and ionization of N_2, respectively. As the electron density increases dramatically during the filament phase, the electric field decreases, causing the decay of $N_2(C^3\Pi_u)$ excitation. In addition, the density of $N_2(C^3\Pi_u)$ decreases due to ionization and dissociation (R7-10, R18-21), and the N_2^+ density decreases by the recombination reaction (R39-41).

Will note that the collisions of electronically excited species between them resulting in production of charged species [73, 74], like Penning ionization or associative ionization, are not important for ionization balance, providing the electron densities a few orders of magnitude lower than the electron densities under the streamer–to–filament transition.

The streamer-to-filament transition is characterized by a fast and sharp increase in electron density. The rates of the dominant ionization processes (figure 11) should be analyzed to understand which reactions contribute to the streamer-to-filament transition. At 9.5 ns, when the ionization wave passes through the probe point, the rates of ionization processes increase dramatically. During the glow phase, the electron production is dominated by the ionization of ground-state N_2 and O_2 (reactions (11) and (12)):

$$e + N_2 => 2e + N_2^+ \tag{11}$$

$$e + O_2 => 2e + O_2^+. \tag{12}$$
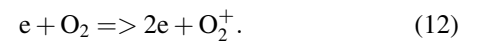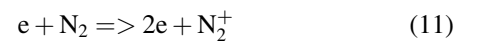
After the conductive channel forms at 9.6 ns, the rates of ionization of excited N_2 (reaction (13)) increase fast, as well as those of ground and excited states of N and O (reactions (14) and (15)).
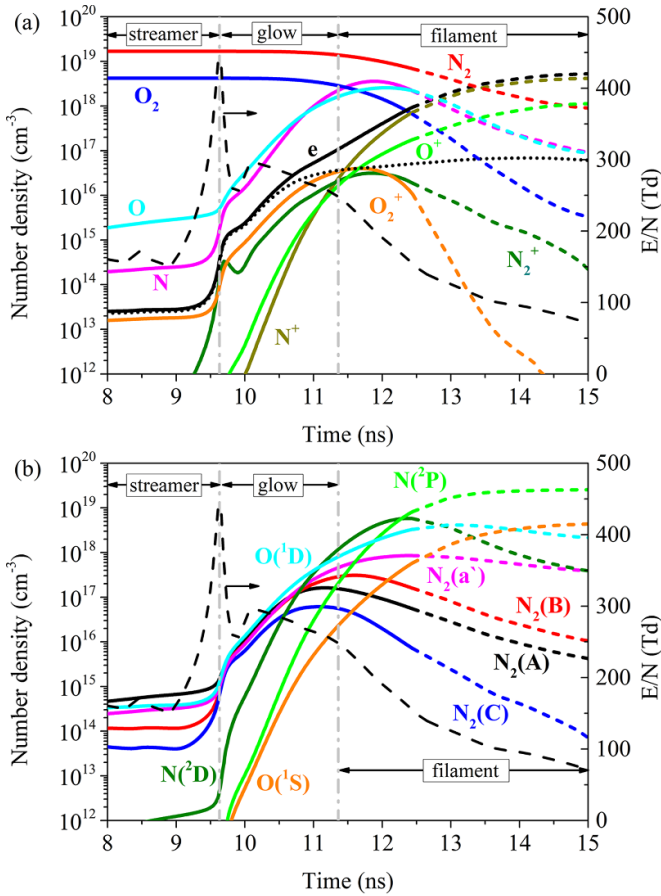
$$e + N_2(A^3{\textstyle\sum_u^+}, B^3\Pi_g, a'^1{\textstyle\sum_u^-}, C^3\Pi_u) => 2e + N_2^+ \tag{13}$$

$$e + N(^4S, ^2D, ^2P) => 2e + N^+ \tag{14}$$

Figure 11. Rates of the main reactions responsible for the production of electrons near the cathode ($r = 0$, $z = 0.05$ mm). The bold solid curves refer to times when $n_e \leqslant 10^{18}$ cm^{-3}, and short dashed curves indicate when $n_e \geqslant 10^{18}$ cm^{-3}. The black line represents the electron density plotted as a reference.

Figure 10. Kinetic curves of selected (a) ground and charged, and (b) excited species close to the cathode ($r = 0$, $z = 0.05$ mm). The bold solid curves refer to times when $n_e \leqslant 10^{18}$ cm^{-3}, and short dashed curves indicate when $n_e \geqslant 10^{18}$ cm^{-3}. The dotted black line in (a) is the electron density without consideration of reactions (13)–(15) (shown below). The reduced electric field strength is plotted as a reference.

$$e + O(^3P, {}^1D, {}^1S) => 2e + O^+. \tag{15}$$
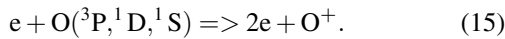
During the filament phase ($t > 11.3$ ns), the rates of ionization of ground N$_2$ and O$_2$ decrease fast due to the fast decay of N$_2$ and O$_2$ number densities during this time (see figure 10). Instead, electrons are mainly produced by ionization reactions ((13)–(15)). Thus, ionization via electronically excited states of atoms dominates charge production in the filament.

The importance of such stepwise ionization was also reported for the streamer-to-filament transition in SDBDs [18, 75]. Due to the higher cross sections of ionization of electronically excited states, the ionization rate coefficients are orders of magnitude larger than those of direct ionization of the ground state species [46]. Hence, as the number densities of these electronically excited states increase, stepwise ionization plays an increasingly important role. In the case of diatomic molecules, electronically excited states can be easily dissociated and ionized. The produced atoms are rapidly excited by electron impact and furthermore ionized. The increase in electron density leads to more ionization and dissociation of
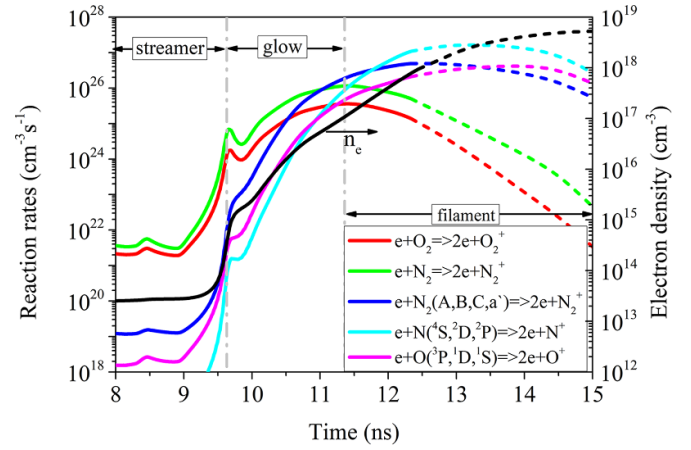
the ground and excited states of molecules, leading to positive feedback and unstable behavior.

With reactions (13)–(15) excluded from the simulation, the calculated electron density as a function of time near the cathode is shown with a dotted black line in figure 10(a). By $t = 15$ ns, the electron density obtained without stepwise ionization becomes nearly two orders of magnitude lower than with the inclusion of this process. Thus, neglecting these reactions fails to reproduce the transition. However, before $t = 10$ ns the results are identical, showing that these reactions do not have any effect on the calculation during the streamer phase.

4.5. Fast gas heating

Experimental temperature measurements in a transient discharge are usually carried out in two ways [16, 21, 38]. At the stage of the glow, the gas temperature is measured by the distribution of radiation over the rotational levels of the second positive system of nitrogen, and the values do not exceed 1000–1500 K. At the stage of the filament and thermal spark, the electron temperature is measured by the relative intensity of selected atomic lines (the so-called Boltzmann plot), and the measured values are typically tens of thousands of kelvins, e.g. ~30000–60000 K. These two measurements are separated by only a few nanoseconds.

At the glow stage, the gas temperature rises due to the collisional relaxation of the energy of electronically excited states of atoms and molecules (the so-called fast gas heating effect or FGH [76]). With an increase in the degree of ionization during the filament/thermal spark stage, elastic electron–ion collisions become the main fast heating mechanism [69], with a characteristic thermalization time depending on the electron density. For an electron density of $n_e \approx 10^{17}$ cm^{-3}, the electron–ion thermalization time is $\tau_{ei} \approx 100$ ns [19], which is much longer than the timescale of the streamer-to-filament transition.
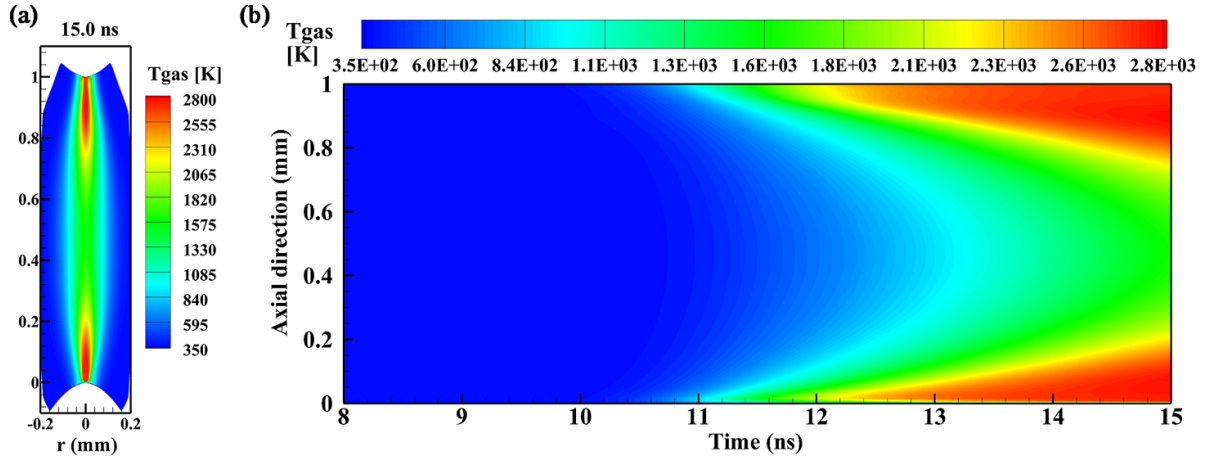
Figure 12. (a) The gas temperature distribution at 15 ns. (b) The time evolution of the gas temperature along the axis $r = 0$.

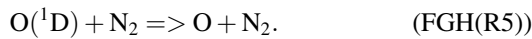In the present work, the main reactions describing fast gas heating are the following:

$$e + O_2 => e + O + O/O(^1D) \qquad \text{(FGH(R1))}$$

$$N_2(B^3\Pi_g) + O_2 => N_2 + O + O \qquad \text{(FGH(R2))}$$

$$N_2(C^3\Pi_u) + O_2 => N_2 + O + O/O(^1D) \qquad \text{(FGH(R3))}$$

$$N_2(a'^1\textstyle\sum_u^-) + O => NO + N(^2D) \qquad \text{(FGH(R4))}$$

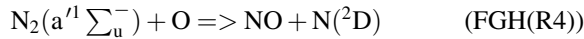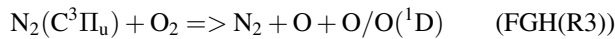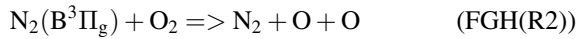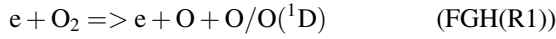$$O(^1D) + N_2 => O + N_2. \qquad \text{(FGH(R5))}$$

Figure 12(a) presents a calculated distribution of gas temperature at 15.0 ns. The calculated streak image of the temperature is shown in figure 12(b). At the center of the gap, the electron density is $n_e \leqslant 10^{17}$ cm^{-3} throughout the considered time interval (see figures 4 and 6), and so the heating in the center of the gap is mainly due to the FGH mechanism. Heating in the near-electrode regions reaches up to $\sim$3000 K in gas temperature, but this is greatly underestimated due to the much higher electron densities that require the consideration of elastic electron-ion collisions.

The calculated temperature is in good qualitative agreement with time- and space-resolved temperature measurements using the rotational spectrum of the $N_2(C^3\Pi_u) \to N_2(B^3\Pi_g)$ transition (figure 67 of [20]). The temperature during the glow phase is practically uniform over the entire discharge gap, with a weakly pronounced minimum in the center of the gap; relatively narrow temperature maxima are observed in the near-electrode regions. As the streamer-filament transition develops, the emission of molecular nitrogen from the near-electrode regions disappears, in full accordance with the spatial distributions of the electric field and the densities of the excited molecules described in the previous section.

The emission intensity from a rotational level is proportional to the product of the density of molecules in this level by the Einstein coefficient of the observed line. The density of

molecules is an exponentially decaying function of rotational temperature, $n_J \sim e^{-E_J/kT_{\rm rot}}$. To enable a quantitative comparison between the computed and measured gas temperatures, it is essential to take into account both (i) the spatial distribution of the temperature field and (ii) the spatial distribution and geometry of radiation collection.

Let at each point of space r_i the rotational temperature is $T_{\rm rot}(r_i) = T_i$. Similar to [77], will consider the sum of the exponential distributions $a_i e^{-E/kT_i}$ with the same rotational energy E and different temperatures T_i with weights a_i (at constrain $\sum a_i = 1$). The rotational energy $E = BJ(J+1)$ with rotational quantum number J and rotational constant B is much smaller than kT, since a typical value of B corresponds to few Kelvins ($B/k = 2.626$ K for the $N_2(C^3\Pi_u)$ state). The last condition means that $E \ll kT$ even at room temperature, and using the Taylor expansion,

$$\sum a_i e^{-\frac{E}{kT_i}} \approx \sum a_i \left(1 - \frac{E}{kT_i} \right) = 1 - \frac{E}{k} \cdot \sum \frac{a_i}{T_i} \approx e^{\frac{E}{kT_{\rm eff}}} \tag{16}$$

with the effective temperature $T_{\rm eff}$ defined as

$$\frac{1}{T_{\rm eff}} = \sum \frac{a_i}{T_i}. \tag{17}$$

The last expression means that the sum of the exponential distributions can in our case be considered as exponential distribution with an effective temperature $T_{\rm eff}$.

In the discharge, the temperature and the number of emitting $N_2(C^3\Pi_u)$ molecules varies continuously, so the integration and convolution of (16) and (17) with the radial profile of emitting particles is required. In the experiments (figure 21 of [20]), the discharge is aligned along the input slit of the spectrometer and only a narrow near-axis zone is observed. At the same time, in the plane perpendicular to the slit of the spectrometer, the emission is integrated over the diameter of the discharge. So we used a plane approximation of the region of the collection of emission, and the integration was performed in the following way:
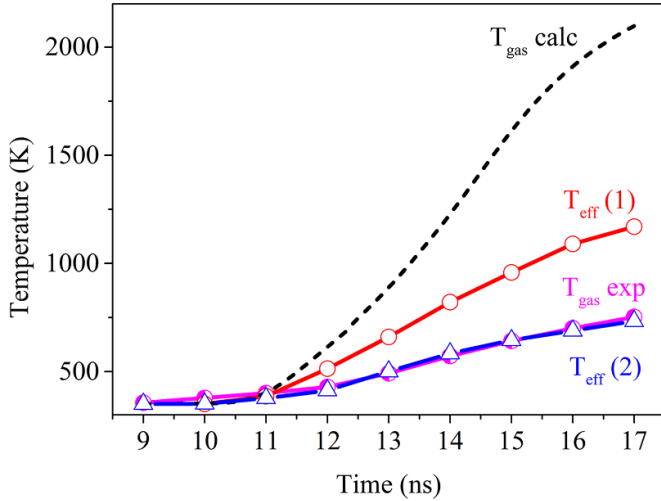
Figure 13. Comparison of calculated non-convoluted T_{gas} (calc), calculated convoluted over the region of measurements (T_{eff} (1,2) - see text for the details) and the experimentally measured T_{gas}(exp) (figure 67 of [20]) gas temperatures at the probe point $r = 0$, $z = 0.5$ mm.

$$\frac{1}{T_{eff}} = \frac{1}{\int_{-R_0}^{R_0} [\mathrm{N_2(C)}](r)\,dr} \int_{-R_0}^{R_0} \frac{[\mathrm{N_2(C)}](r)\,dr}{T_{rot}(r)}, \qquad (18)$$

where $\mathrm{N_2(C)}$ means $\mathrm{N_2(C^3\Pi_u)}$.

As it was mentioned in the section 2, in our particular case the rotational-translational relaxation is fast comparing to the lifetime, the emitting molecules are in the thermodynamic equilibrium with surrounding gas and the measured rotational temperature is equal to the gas temperature, $T_{rot} = T_{gas}$.

Figure 13 provides a comparison of calculated non-convoluted T_{gas}(calc), calculated convoluted over the region of measurements T_{eff} and the experimentally measured gas temperatures at the probe point $r = 0$, $z = 0.5$ mm. The difference between T_{eff} (1) and T_{eff} (2) is that in the second case it was assumed that a significant part of energy (90%) in reactions (R81), (R86) and (R89) goes to the vibrational excitation of NO(v) without immediate energy release to heat. Indeed, although the VT-relaxation of NO(v) on O–atoms is fast (the rate constant is 6.5×10^{-11} cm^{3}s^{-1} [24]), under present conditions a typical VT-relaxation time can be estimated as 50 ns, higher than the calculation time.

A good agreement, in time and space, between the calculated and measured temperatures during the glow phase can be considered as an additional validation of the presented 2D model.

4.6. Memory effect

Experiments have demonstrated that the streamer-to-filament transition is enhanced by the memory effect of repetitive pulses. Preheating and changes to the gas composition induced by previous pulses can influence the streamer-to-filament transition by contributing to the acceleration of the ionization process, for example via stepwise ionization and dissociation
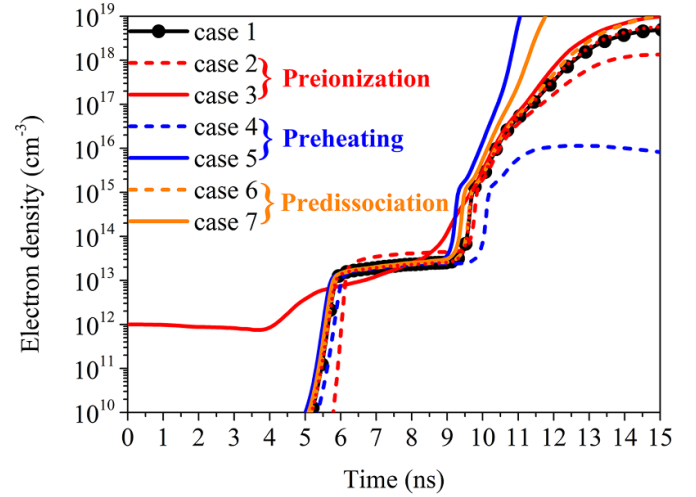

Figure 14. The temporal profiles of electron density at the probe point $r = 0$, $z = 0.05$ mm for the different cases shown in table 2.

Table 2. Different hypothetical cases of preionization, preheating, and predissociation due to the memory effect between pulses.

Case	n_{e0}, cm^{-3}	T_{gas}, K	$n_N = n_O$, cm^{-3}
Case 1	10^9	350	10^1
Case 2	10^6	350	10^1
Case 3	10^{12}	350	10^1
Case 4	10^9	320	10^1
Case 5	10^9	380	10^1
Case 6	10^9	350	10^{17}
Case 7	10^9	350	10^{18}

[78]. Moreover, the ions and electrons left after previous pulses can also contribute to the transition from a stable diffuse mode to a filament [79].

To investigate the influence of the memory effect (i.e. preheating, preionization, and predissociation) on the streamer-to-filament transition, 7 cases with different initial conditions are compared. Case 1 is the reference with the initial conditions used to produce all of the above results in this paper. Relative to case 1, one initial parameter is changed for each of the other cases. Figure 14 shows the electron density evolution near the cathode for different initial conditions. The electron density is chosen intentionally as a parameter of comparison. First, the electron density is one of the key parameters that determine the properties of gas-discharge plasma. Second, the sharp increase of electron density indicates the beginning of transition to the filament.

The electron density for the discharge frequency range of 10–100 kHz can reach up to 4.0×10^{11} cm^{-3} [62], so it is important to investigate the influence of such a high degree of preionization on the discharge dynamics. The curves for the cases 1, 2, and 3 show the electron density evolution for three different preionization levels. Increasing the preionization causes the electron density to increase more rapidly, thus accelerating the transition. Still the influence of the initial electron density on the transition is not dramatic: changing the initial electron density by 6 orders of magnitude, between

10^6 cm^{-3} and 10^{12} cm^{-3} leads to the change of $n_e(t)$ withing only one order of magnitude at $t = 15$ ns. Will note that the decay of plasma in the filament is relatively slow and the characteristic time of this decay will be determined by the cooling time of the gas in hot channel. In the middle of the discharge gap, the main source of electrons in the afterglow is the destruction of negative ions by O-atoms produced in the discharge. Hence, the effect of negative ions is equivalent to maintaining the initial electron density value from pulse to pulse, and the sensitivity of the problem to the initial n_e density is weak.

Preheating has a great effect on the transition, as demonstrated by comparing cases 1, 4, and 5. A higher initial temperature strongly promotes the transition, while at a lower temperature of 320 K, the transition does not occur. For example, in the experiment [78], when the gas in the discharge gap was heated to 1000 K by previous pulses, a very short spark current pulse appeared. Higher gas temperature decreases the gas density, which causes an increase in E/N, accelerating the crossing of the streamer and the transition [33].

Changes in the gas composition caused by previous pulses can also contribute to the streamer-to-filament transition. From the rate analysis above, the ionization of excited levels of N$_2$, N, and O greatly contributes to the transition. The lifetime of excited species is short, but ground-state atoms like O can survive a long time during the afterglow [52, 80]. Here, we only discuss the predissociation of N$_2$ and O$_2$, that is to say the effect of the initial values of N- and O-atoms on the transition, which can be seen by the curves for cases 1, 6, and 7. It can be seen that the accumulation of atomic oxygen and nitrogen could promote the ionization process and thus accelerate the transition process. However, a considerable level of predissociation is required to make an appreciable impact.

Summarizing, will note that in this study the highest sensitivity was observed with respect to gas density (the changes in gas density were due to changes in temperature).

5. Conclusions

In the present work, the streamer-to-filament transition in a pin-to-pin configuration in air at atmospheric pressure has been studied by a 2D PASSKEy plasma fluid code. The calculations have been performed for a positive voltage pulse applied across a discharge gap of 1 mm, with 6 kV amplitude and 20 ns duration. A kinetic scheme providing a sharp electron density increase has been established. The model has been validated using experimental data [20] as a benchmark. The electrical parameters, morphology, propagation dynamics, transition mechanism, and fast gas heating have been studied.

According to the experimental measurements, the electron density at the end of the pulse exceeds 1.0×10^{19} cm^{-3}, reaching a thermal-spark phase. However, the main research object of this paper is the streamer-to-filament transition, which precedes the thermal spark.

The streamer-to-filament transition is characterized by a sharp increase in electron density, fast increase of gas temperature, and appearance of a thin highly conductive channel on the axis of the discharge. At the beginning of the discharge development, a positive streamer and a 'corona-like' negative streamer propagate towards the middle of the gap and merge with each other, forming a homogeneous conductive channel with an electron density of 1.0×10^{14} cm^{-3} and reduced electric field of 250 Td. Then, cathode- and anode-directed filaments originate at the anode and cathode, respectively, and propagate towards the middle of the gap with a velocity of about 1.1×10^7 cm s^{-1}. They merge into a narrow discharge channel, with an electron density of 1.0×10^{17} cm^{-3} at the gap center and 5.0×10^{18} cm^{-3} near the electrodes. Simultaneously, the gas temperature increases by thousands of K. The channel constriction first appears near the electrodes, then in the rest of the discharge gap. The channel diameter, defined as the FWHM of the radial distribution of the electron density, reduces from 60–90 to 10–20 μm near the electrodes, and from 200 to 80 μm at the center of the gap.

During the transition, the plasma abruptly changes from molecular to almost atomic in composition, and the dominant charged species change from N$_2^+$ and O$_2^+$ to N$^+$ and O$^+$. The densities of the electronically excited states of N$_2$ increase during the glow phase due to excitation by direct electron impact and then decrease during the filament phase, when the electric field decreases.

The dissociation and ionization of electronically excited states of molecules N$_2$(A$^3\sum_u^+$, B$^3\Pi_g$, a$'^1\sum_u^-$, C$^3\Pi_u$), as well as the ionization of ground and electronically excited states of atoms N(^{4}S, ^{2}D, ^{2}P) and O(^{3}P, ^{1}D, ^{1}S), are the most important processes for the transition. Neglecting these reactions fails to capture the transition but does not influence the numerical results for the streamer phase.

Calculated fast gas heating describes experimentally measured heat release in time and space during the glow phase. Heating of the gas at high ($\sim 10^{19}$ cm^{-3}) electron densities should be calculated with account of elastic electron–ion collisions which is beyond the scope of this paper.

The memory effect from previous pulses has a significant effect on the streamer-to-filament transition. Between preionization, predissociation, and preheating, the latter is the most influential. Changing the initial gas temperature changes the gas density, thus altering the reduced electric field and the reactions of ionization.

Data availability statement

All data that support the findings of this study are included within the article (and any supplementary files).

ORCID iDs

Bin Zhang ⓘ https://orcid.org/0000-0001-8126-8073
Yifei Zhu ⓘ https://orcid.org/0000-0001-8989-0051
Xiaobing Zhang ⓘ https://orcid.org/0000-0003-3928-1009
Nikolay Popov ⓘ https://orcid.org/0000-0001-8738-9642
Thomas Orriere ⓘ https://orcid.org/0000-0002-9278-7124
David Z Pai ⓘ https://orcid.org/0000-0002-1748-1950
Svetlana M Starikovskaia ⓘ https://orcid.org/0000-0001-6954-7336

References

[1] Nijdam S, Teunissen J and Ebert U 2020 The physics of streamer discharge phenomena (topical review) *Plasma Sources Sci. Technol.* **29** 103001

[2] Pancheshnyi S, Nudnova M and Starikovskii A 2005 Development of a cathode-directed streamer discharge in air at different pressures: experiment and comparison with direct numerical simulation *Phys. Rev.* E **71** 016407

[3] Briels T M P, Kos J, Winands G J J, van Veldhuizen E M and Ebert U 2008 Positive and negative streamers in ambient air: measuring diameter, velocity and dissipated energy *J. Phys. D: Appl. Phys.* **41** 234004

[4] Minesi N, Stepanyan S, Mariotto P, Stancu G D and Laux C 2020 Fully ionized nanosecond discharges in air: the thermal spark *Plasma Sources Sci. Technol.* **29** 085003

[5] Tardiveau P, Moreau N, Bentaleb S, Postel C and Pasquiers S 2009 Diffuse mode and diffuse-to-filamentary transition in a high pressure nanosecond scale corona discharge under high voltage *J. Phys. D: Appl. Phys.* **42** 175202

[6] Shcherbanev S A, Khomenko A Y, Stepanyan S A, Popov N A and Starikovskaia S M 2017 Optical emission spectrum of filamentary nanosecond surface dielectric barrier discharge *Plasma Sources Sci. Technol.* **26** 02LT01

[7] Janda M, Martišovitš V, Hensel K, Dvonc L and Machala Z 2014 Measurement of the electron density in transient spark discharge *Plasma Sources Sci. Technol.* **23** 065016

[8] Lo A, Cessou A, Lacour C, Lecordier B, Boubert P, Xu D, Laux C and Vervisch P 2017 Streamer-to-spark transition initiated by a nanosecond overvoltage pulsed discharge in air *Plasma Sources Sci. Technol.* **26** 045012

[9] Horst R M V D, Verreycken T, Veldhuizen E M V and Bruggeman P J 2012 Time-resolved optical emission spectroscopy of nanosecond pulsed discharges in atmospheric-pressure N_2 and N_2/H_2O mixtures *J. Phys. D: Appl. Phys.* **45** 345201

[10] Minesi N, Stepanyan S A, Mariotto P B, Stancu G D and Laux C O 2019 On the arc transition mechanism in nanosecond air discharges *2019 AIAA SciTech Forum (San Diego, California, 7–11 January 2019)* p AIAA paper 2019-0463

[11] Naidis G V 1999 Simulation of streamer-to-spark transition in short non-uniform air gaps *J. Phys. D: Appl. Phys.* **32** 2649–54

[12] Tholin F and Bourdon A 2011 Influence of temperature on the glow regime of a discharge in air at atmospheric pressure between two point electrodes *J. Phys. D: Appl. Phys.* **44** 385203

[13] Tholin F and Bourdon A 2013 Simulation of the hydrodynamic expansion following a nanosecond pulsed spark discharge in air at atmospheric pressure *J. Phys. D: Appl. Phys.* **46** 365205

[14] Lo A, Cessou A, Boubert P and Vervisch P 2014 Space and time analysis of the nanosecond scale discharges in atmospheric pressure air: I. Gas temperature and vibrational distribution function of N_2 and O_2 *J. Phys. D: Appl. Phys.* **47** 115201

[15] Stepanyan S, Starikovskiy A Y, Popov N and Starikovskaia S 2014 A nanosecond surface dielectric barrier discharge in air at high pressures and different polarities of applied pulses: transition to filamentary mode *Plasma Sources Sci. Technol.* **23** 045003

[16] Ding C, Khomenko A Y, Shcherbanev S and Starikovskaia S 2019 Filamentary nanosecond surface dielectric barrier discharge. Experimental comparison of the streamer-to-filament transition for positive and negative polarities *Plasma Sources Sci. Technol.* **28** 085005

[17] Ding C, Jean A, Popov N A and Starikovskaia S M 2022 Fine structure of streamer-to-filament transition in high-pressure nanosecond surface dielectric barrier discharge *Plasma Sources Sci. Technol.* **31** 045013

[18] Shcherbanev S, Ding C, Starikovskaia S and Popov N 2019 Filamentary nanosecond surface dielectric barrier discharge. Plasma properties in the filaments *Plasma Sources Sci. Technol.* **28** 065013

[19] Minesi N, Mariotto P, Pannier E, Stancu G and Laux C 2021 The role of excited electronic states in ambient air ionization by a nanosecond discharge *Plasma Sources Sci. Technol.* **30** 035008

[20] Orrière T 2018 Confinement micrométrique des décharges pulsées nanosecondes dans l'air à pression atmosphérique et effets électro-aérodynamiques *PhD Thesis* Université de Poitiers (in French)

[21] Orrière T, Moreau E and Pai D Z 2018 Ionization and recombination in nanosecond repetitively pulsed microplasmas in air at atmospheric pressure *J. Phys. D: Appl. Phys.* **51** 494002

[22] Laux C O, Spence T, Kruger C and Zare R 2003 Optical diagnostics of atmospheric pressure air plasmas *Plasma Sources Sci. Technol.* **12** 125

[23] Voráč J, Synek P, Potočňáková L, Hnilica J and Kudrle V 2017 Batch processing of overlapping molecular spectra as a tool for spatio-temporal diagnostics of power modulated microwave plasma jet *Plasma Sources Sci. Technol.* **26** 025010

[24] Capitelli M, Ferreira C M, Gordiets B F and Osipov A 2000 *Plasma Kinetics in Atmospheric Gases* (Springer) (https://doi.org/10.1007/978-3-662-04158-1)

[25] Rusterholtz D, Lacoste D, Stancu G, Pai D and Laux C 2013 Ultrafast heating and oxygen dissociation in atmospheric pressure air by nanosecond repetitively pulsed discharges *J. Phys. D: Appl. Phys.* **46** 464010

[26] Bruggeman P J, Sadeghi N, Schram D C and Linss V 2014 Gas temperature determination from rotational lines in non-equilibrium plasmas: a review *Plasma Sources Sci. Technol.* **23** 023001

[27] Lavrov B P, Ostrovsky V N and Ustimov V I 1979 Rotational transitions in the excitation of electronic states of molecules by electron impact *Sov. Phys. JETP* **49** 772–6

[28] Zhu Y, Shcherbanev S, Baron B and Starikovskaia S 2017 Nanosecond surface dielectric barrier discharge in atmospheric pressure air: I. Measurements and 2D modeling of morphology, propagation and hydrodynamic perturbations *Plasma Sources Sci. Technol.* **26** 125004

[29] Zhu Y and Starikovskaia S M 2018 Fast gas heating of nanosecond pulsed surface dielectric barrier discharge: spatial distribution and fractional contribution from kinetics *Plasma Sources Sci. Technol.* **27** 124007

[30] Zhu Y, Wu Y, Wei B, Liang H, Jia M, Song H, Haojun X and Li Y 2019 Nanosecond-pulsed dielectric barrier discharge-based plasma-assisted anti-icing: modeling and mechanism analysis *J. Phys. D: Appl. Phys.* **53** 145205

[31] Zhu Y and Wu Y 2020 The secondary ionization wave and characteristic map of surface discharge plasma in a wide time scale *New J. Phys.* **22** 103060

[32] Kulikovsky A 1998 Positive streamer in a weak field in air: a moving avalanche-to-streamer transition *Phys. Rev.* E **57** 7066

[33] Chen X, Zhu Y and Wu Y 2020 Modeling of streamer-to-spark transitions in the first pulse and the post discharge stage *Plasma Sources Sci. Technol.* **29** 095006

[34] Zhu Y, Chen X, Wu Y, Hao J, Ma X, Lu P and Tardiveau P 2021 Simulation of ionization-wave discharges: a direct comparison between the fluid model and E-FISH measurements *Plasma Sources Sci. Technol.* **30** 075025

[35] Bourdon A, Pasko V, Liu N, Célestin S, Ségur P and Marode E 2007 Efficient models for photoionization produced by non-thermal gas discharges in air based on radiative transfer and the Helmholtz equations *Plasma Sources Sci. Technol.* **16** 656–78

[36] Hagelaar G J M and Pitchford L C 2005 Solving the Boltzmann equation to obtain electron transport coefficients and rate coefficients for fluid models *Plasma Sources Sci. Technol.* **14** 722–33

[37] Laux C O, Yu L, Packan D M, Gessman R J, Pierrot L, Kruger C H and Zare R N 1999 Ionization mechanisms in two-temperature air plasmas *30th Plasmadynamic and Lasers Conf.* (*Reston, Virigina American Institute of Aeronautics and Astronautics*) pp 99–3476

[38] Minesi N 2020 Thermal spark formation and plasma-assisted combustion by nanosecond repetitive discharges *PhD Thesis* Université Paris-Saclay (in French)

[39] ZDPlasKin 2008 (available at: www.zdplaskin.laplace.univ-tlse.fr/)

[40] Zhu Y, Lepikhin N D, Orel I S, Salmon A, Klochko A V and Starikovskaia S M 2018 Optical actinometry of O-atoms in pulsed nanosecond capillary discharge: peculiarities of kinetics at high specific deposited energy *Plasma Sources Sci. Technol.* **27** 075020

[41] Isola L M, Gomez B J and Guerra V 2010 Determination of the electron temperature and density in the negative glow of a nitrogen pulsed discharge using optical emission spectroscopy *J. Phys. D: Appl. Phys.* **43** 015202

[42] Itikawa Y 2009 Cross sections for electron collisions with oxygen molecules *J. Phys. Chem. Ref. Data* **38** 1–20

[43] Itikawa Y 2016 Cross sections for electron collisions with nitric oxide *J. Phys. Chem. Ref. Data* **45** 033106

[44] Tayal S S and Zatsarinny O 2016 B -spline R -matrix-with-pseudostates approach for excitation and ionization of atomic oxygen by electron collisions *Phys. Rev.* A **94** 1–15

[45] Wang Y, Zatsarinny O and Bartschat K 2014 B-spline R-matrix-with-pseudostates calculations for electron-impact excitation and ionization of nitrogen *Phys. Rev.* A **89** 062714

[46] Bacri J and Medani A 1982 Electron diatomic molecule weighted total cross section calculation *Physica* B+C **112** 101–18

[47] Phelps A V 1985 *Report 28 JILA Information Center* University of Colorado

[48] Cosby P C 1993 Electron-impact dissociation of nitrogen *J. Chem. Phys.* **98** 9544–53

[49] Popov N A 2013 Dissociation of nitrogen in a pulse-periodic dielectric barrier discharge at atmospheric pressure *Plasma Phys. Rep.* **39** 420–4

[50] Pitchford L C and Phelps A V 1982 Comparative calculations of electron-swarm properties in N_2 at moderate E/N values *Phys. Rev.* A **25** 540–54

[51] Lawton S and Phelps A V 1978 Excitation of the $b^1\Sigma_g^+$ state of O_2 by low energy electrons *J. Chem. Phys.* **69** 1055–68

[52] Mintoussov E I, Pendleton S J, Gerbault F G, Popov N A and Starikovskaia S M 2011 Fast gas heating in nitrogen–oxygen discharge plasma: II. Energy exchange in the afterglow of a volume nanosecond discharge at moderate pressures *J. Phys. D: Appl. Phys.* **44** 285202

[53] Popov N 2011 Fast gas heating in a nitrogen–oxygen discharge plasma: I. Kinetic mechanism *J. Phys. D: Appl. Phys.* **44** 285201

[54] Park C 1993 Review of chemical-kinetic problems of future NASA missions, I- Earth entries *J. Thermophys. Heat Transfer* **7** 385–98

[55] Starik A M, Titova N S and Arsentiev I V 2010 Comprehensive analysis of the effect of atomic and molecular metastable state excitation on air plasma composition behind strong shock waves *Plasma Sources Sci. Technol.* **19** 015007

[56] Kossyi I, Kostinsky A Y, Matveyev A and Silakov V P 1992 Kinetic scheme of the non-equilibrium discharge in nitrogen-oxygen mixtures *Plasma Sources Sci. Technol.* **1** 207

[57] Thomas J M and Kaufman F 1996 An upper limit on the formation of $NO(X^2\Pi_r)$ in the reactions $N_2(A^3\sum_u^+)+O(^3P)$ and $N_2(A^3\sum_u^+)+O_2(X^3\sum_g^-)$ at 298 K *J. Phys. Chem.* **100** 8901–6

[58] Shkurenkov I, Burnette D, Lempert W R and Adamovich I V 2014 Kinetics of excited states and radicals in a nanosecond pulse discharge and afterglow in nitrogen and air *Plasma Sources Sci. Technol.* **23** 065003

[59] Kobayashi S, Bonaventura Z, Tholin F, Popov N and Bourdon A 2017 Study of nanosecond discharges in H_2–air mixtures at atmospheric pressure for plasma assisted combustion applications *Plasma Sources Sci. Technol.* **26** 075004

[60] Piper L G 1987 Quenching rate coefficients for $N_2(a'^1\sum_u^-)$ *J. Chem. Phys.* **87** 1625–9

[61] Galvão B R L, Varandas A J C, Braga J P and Belchior J C 2013 Electronic quenching of $N(^2D)$ by N_2: theoretical predictions, comparison with experimental rate constants and impact on atmospheric modeling *J. Phys. Chem. Lett.* **4** 2292–7

[62] Tholin F and Bourdon A 2013 Simulation of the stable 'quasi-periodic' glow regime of a nanosecond repetitively pulsed discharge in air at atmospheric pressure *Plasma Sources Sci. Technol.* **22** 045014

[63] Eichwald O, Ducasse O, Dubois D, Abahazem A, Merbahi M and Yousfi M 2008 Experimental analysis and modelling of positive streamer in air: towards an estimation of O and N radical production *J. Phys. D: Appl. Phys.* **41** 234002

[64] Ono R and Komuro A 2020 Generation of the single-filament pulsed positive streamer discharge in atmosphericpressure

air and its comparison with two-dimensional simulation *J. Phys. D: Appl. Phys.* **53** 035202

[65] Komuro A, Ono R and Oda T 2013 Effects of pulse voltage rise rate on velocity, diameter and radical production of an atmospheric-pressure streamer discharge *Plasma Sources Sci. Technol.* **22** 045002

[66] Hagelaar G J M 2016 Coulomb collisions in the Boltzmann equation for electrons in low-temperature gas discharge plasmas *Plasma Sources Sci. Technol.* **25** 015015

[67] Celestin S, Bonaventura Z, Zeghondy B, Bourdon A and Segur P 2009 The use of the ghost fluid method for Poisson's equation to simulate streamer propagation in point-to-plane and point-to-point geometries *J. Phys. D: Appl. Phys.* **42** 065203

[68] Bruggeman P J, Iza F and Brandenburg R 2019 Foundations of atmospheric pressure non-equilibrium plasmas *Plasma Sources Sci. Technol.* **26** 123002

[69] Raizer Y P 1991 *Gas Discharge Physics* 2nd edn (Springer) (https://doi.org/10.1007/978-3-642-61247-3)

[70] Sigmond R S 1984 The residual streamer channel: return strokes and secondary streamers *J. Appl. Phys.* **56** 1355–70

[71] Marode E, Djermoune D, Dessante P, Deniset C, Segur P, Bastien F, Bourdon A and Laux C 2009 Physics and applications of atmospheric non-thermal air plasma with reference to environment *Plasma Phys. Control. Fusion* **51** 124002

[72] Janda M, Machala Z, Niklova A and Martisovits V 2012 The streamer-to-spark transition in a transient spark: a dc-driven nanosecond-pulsed discharge in atmospheric air *Plasma Sources Sci. Technol.* **21** 045006

[73] Guerra V and Loureiro J 2004 Kinetic modeling of low-pressure nitrogen discharges and post-discharges *Eur. Phys. J. Appl. Phys.* **28** 125–52

[74] Popov N A 2009 Associative ionization reactions involving excited atoms in nitrogen plasma *Plasma Phys. Rep.* **35** 436–49

[75] Soloviev V R 2022 Filament formation mechanism for a nanosecond surface barrier discharge of positive polarity in nitrogen *Plasma Phys. Rep.* **48** 669–81

[76] Popov N A and Starikovskaia S M 2022 Relaxation of electronic excitation in nitrogen/oxygen and fuel/air mixtures: fast gas heating in plasma-assisted ignition and flame stabilization *Prog. Energy Combust. Sci.* **91** 100928

[77] Lepikhin N D, Popov N A and Starikovskaia S M 2018 Fast gas heating and radial distribution of active species in nanosecond capillary discharge in pure nitrogen and N_2:O_2 mixtures *Plasma Sources Sci. Technol.* **27** 055005

[78] Janda M, Martišovitš V, Buček A, Hensel K, Molnár M and Machala Z 2017 Influence of repetition frequency on streamer-to-spark breakdow mechanism in transient spark discharge *J. Phys. D: Appl. Phys.* **50** 425207

[79] Shao T, Zhang C, Niu Z, Yan P, Tarasenko V F, Baksht E K, Burahenko A G and Shut'ko Y V 2011 Diffuse discharge, runaway electron and x-ray in atmospheric pressure air in an inhomogeneous electrical field in repetitive pulsed modes *Appl. Phys. Lett.* **91** 021503

[80] Popov N A 2016 Pulsed nanosecond discharge in air at high specific deposited energy: fast gas heating and active particle production *Plasma Sources Sci. Technol.* **25** 044003